



HAL
open science

In silico experiments of intimal hyperplasia development: disendothelization in an axisymmetric idealized artery

Jérôme Jansen, Xavier Escriva, Fabien Godeferd, Patrick Feugier

► To cite this version:

Jérôme Jansen, Xavier Escriva, Fabien Godeferd, Patrick Feugier. In silico experiments of intimal hyperplasia development: disendothelization in an axisymmetric idealized artery. *Biomechanics and Modeling in Mechanobiology*, 2023, 10.1007/s10237-023-01720-7 . hal-04085178v2

HAL Id: hal-04085178

<https://hal.science/hal-04085178v2>

Submitted on 18 May 2023

HAL is a multi-disciplinary open access archive for the deposit and dissemination of scientific research documents, whether they are published or not. The documents may come from teaching and research institutions in France or abroad, or from public or private research centers.

L'archive ouverte pluridisciplinaire **HAL**, est destinée au dépôt et à la diffusion de documents scientifiques de niveau recherche, publiés ou non, émanant des établissements d'enseignement et de recherche français ou étrangers, des laboratoires publics ou privés.

In silico experiments of intimal hyperplasia development : disendothelization in an axisymmetric idealized artery

Jérôme Jansen · Xavier Escriva · Fabien Godeferd · Patrick Feugier

Received: 31 August 2022 / Accepted: 9 April 2023

Abstract We use *in silico* experiments to study the role of the hemodynamics and of the type of disendothelization on the physiopathology of intimal hyperplasia. We apply a multiscale bio-chemo-mechanical model of intimal hyperplasia on an idealized axisymmetric artery that suffers two kinds of disendothelizations. The model predicts the spatio-temporal evolution of the lesions development, initially localized at the site of damages, and after few days displaced downstream of the damaged zones, these two stages being observed whatever the kind of damage. Considering macroscopic quantities, the model sensitivity to pathology-protective and pathology-promoting zones is qualitatively consistent with experimental findings. The simulated pathological evolutions demonstrate the central role of two parameters: (a) the initial damage shape on the morphology of the incipient stenosis, and (b) the local wall shear stresses on the overall spatio-temporal dynamics of the lesion.

Keywords Intimal hyperplasia, Growth and Remodelling, Hemodynamics, Wall Shear Stress, Multiscale modeling

Funding : No funding was received to assist with the preparation of this manuscript.

Competing interests : The authors have no conflicts of interest to declare that are relevant to the content of this article.

Code availability : All simulation has been achieved with in-house Python packages <https://gitlab.com/jrme.jansen/pytg/>. Python codes used in this study will be available after publication on the gitlab repository.

Authors' contributions : X. Escriva and P. Feugier set up the relevant framework for tackling the modelling of the physiological-mechanical pathology. J. Jansen developed the model and code in axisymmetric configuration, carried out simulations and wrote the manuscript. F. Godeferd, X. Escriva and P. Feugier participated in the discussion of the results. J. Jansen and F. Godeferd wrote the first draft of manuscript.

Ethics approval : This article does not present research with ethical considerations.

Consent to participate : All the authors consented to participate in this study.

Consent for publication : All authors proof-read and consent for the publication of the manuscript.

J. Jansen · X. Escriva · F.S. Godeferd
Laboratoire de Mécanique des Fluides et d'Acoustique, UMR 5509, Univ Lyon, École Centrale de Lyon, INSA Lyon, Université Claude Bernard Lyon I, CNRS, 36 Avenue Guy de Colongue, 69134 Ecully, France
E-mail: jrme.jansen@gmail.com

P. Feugier
Service de Chirurgie Vasculaire et Endovasculaire, LYVES Groupement Hospitalo-Universitaire Lyon Sud, Université Claude Bernard Lyon 1, 69100, Villeurbanne, France

1 Introduction

Intimal hyperplasia (IH) is a thickening of the intima layer of blood vessel resulting from a tissue growth. Subbotin [18] define an IH lesion as “*any cells that form a multi-layer compartment internally to the elastic membrane of the arterial wall and express alpha-smooth-muscle actin, permanently or transitionally*”. Macroscopically, IH causes a reduction in the luminal section of a blood vessel which can lead to its obstruction. At the tissue level, this pathology results from a cascade of biological processes causing a structural rearrangement of the intimal layers of the vascular wall.

Hemodynamics is known to modulate the development of intimal hyperplasia. Although the relationship between vascular adaptation and local hemodynamics has been described for over a century [2], it was in the 1980s that evidence for a relationship between vascular disease development and hemodynamics was obtained [8]. We refer to the review of Peiffer et al. [15] for a detailed history of the influence of hemodynamics on pathological development. Nowadays, the concept that disturbed local hemodynamics is a key factor in the development of vascular lesions — with an inverse correlation between lesion thickness and wall shear stress — is widely accepted [20, 15]. However, Peiffer et al. [15] noticed that “*the evidence for it (theory) is less clear-cut than might at first appear*”.

Despite several decades of high-level medicine research field to understand and treat the onset of intimal hyperplasia through animal models, *in vitro* and *in vivo* studies, much remains to be understood [18]. As “*No new conceptual ideas seem to have arisen during the past 50–60 years of study of arterial neointimal formation*” [18], we observe in literature more and more *in silico* studies which propose mathematical model of multiple vascular pathologies to test hypotheses or to address unresolved questions about pathologies. Escuer et al. [7] study the process of restenosis following the implantation of a stent by a set of partial differential equation of reaction–diffusion type to model the evolution of the lesion. In the context of tissue-engineered vascular grafts, Khosravi et al. [13] propose a mathematical model of the development of grafts with bio-chemo-mechanical equations. Several studies have proposed mathematical models to predict the spatio-temporal development of various vascular pathologies by considering the coupling with blood flow : Cilla et al. [4], Calvez et al. [1] and Corti et al. [5] for atherosclerosis, Goodman et al. [10] and Donadoni et al. [6] for intimal hyperplasia.

Starting from the study of Donadoni et al. [6], we introduced in Jansen et al. [12] a novel multiscale and multiphysics model of intimal hyperplasia in a bio-chemo-

mechanical framework. Our model considers the interactions between hemodynamics, cellular dynamics and biochemistry in a compartmental approach. This mathematical model is based on kinetic differential equations for key vascular species (cellular and non cellular populations) and growth factors. The model was validated on a monodimensional test-case [12].

In the present study, we strictly apply our modelling [12] in a novel geometrical configuration. The main novelty of this work is about the generalization of methods applied to our compartmental modelling into a tridimensional arterial configuration. We present a methodology to manage arterial remodeling in tridimensional configuration which consider a novel algorithm of automatic arterial remodelling with time- and space-dependent detection of remodeling criteria. We consider an application of our modelling in an idealized axisymmetric artery undergoing two different kinds of initial endothelial damage, and we follow the spatio-temporal evolution of the lesions predicted by our model. The aim of the present paper is therefore threefold: (a) we evaluate the response of the model in pathology-protective and pathology-promoting zones described in the literature [15]; (b) we compare the results of one- and tri-dimensional configurations to assess the influence of the geometrical configuration; (c) we explore the influence of the initial endothelial injury on the development of the lesion.

The article is organized as follows. In section 2, we present methods used for computing the model of IH in an axisymmetric idealized artery: in section 2.1, we present the hemodynamics assumptions, equations and numerical methods; in section 2.2, we shortly introduce the model of IH; section 2.3 is devoted to coupling methods in an axisymmetric configuration; finally in section 2.4 we initialize the physiological–damage conditions by defining two types of endothelial damages. Section 3 is devoted to the results and discussion of the spatio-temporal evolutions of lesions. Section 4 reports our main conclusions.

2 Methods

2.1 Hemodynamics modelling

In the luminal domain Ω_1 (see left Figure 1), the blood flow is assumed to be a stationary laminar flow in a rigid duct, whose dynamics is that of an incompressible Newtonian fluid. Hemodynamics is therefore governed

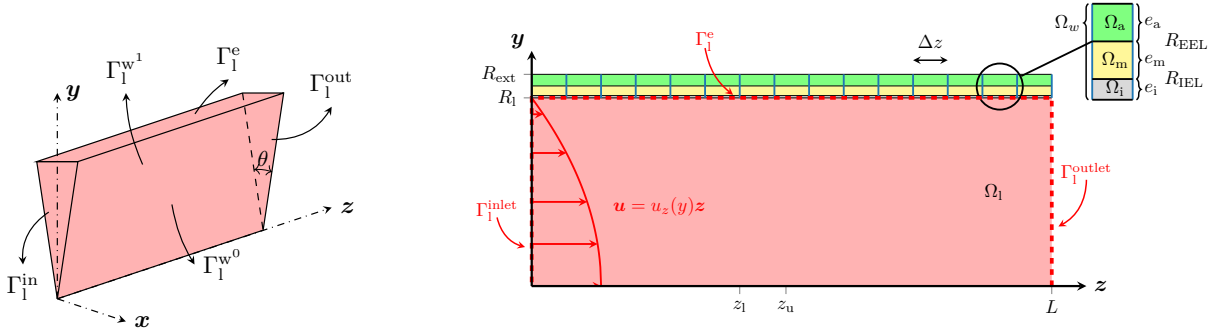


Fig. 1: (Left) Initial luminal domain of a straight axisymmetric artery modelled by a 3D wedge geometry, with wedge angle $\theta = 3^\circ$. Ω_l is the luminal domain delimited by four surfaces: inlet Γ_1^{in} , endothelium wall Γ_1^{e} , outlet Γ_1^{out} and wedge sides $\Gamma_1^{\text{w}0,1}$. (Right) Cut of the considered idealized artery in the symmetry plane (z, y) with z and y respectively the longitudinal and radial directions. The three boundary surfaces are shown in dashed lines. The arterial segment of length L initially suffers a damage of endothelium between z_1 and z_u . The endothelial surface Γ_1^{e} is the interface between lumen and arterial wall at $r = R_1$, the luminal radius. The blow up shows an arterial wall compartment with Ω_i the intima layer of thickness e_i between R_1 and R_{IEL} (radius of internal elastic lamina), Ω_m the media layer of thickness e_m between R_{IEL} and R_{EEL} (radius of external elastic lamina), Ω_a the adventitial layer of thickness e_a between R_{EEL} and R_{ext} (the external radius of the artery). The whole arterial wall domain is noted Ω_w . A uniform parietal mesh is shown with compartments of length Δz (blue vertical lines).

by the Navier–Stokes equations

$$\frac{\partial \mathbf{u}}{\partial t} + (\mathbf{u} \cdot \nabla) \mathbf{u} = -\frac{1}{\rho} \nabla p + \nu \Delta \mathbf{u} \quad \text{in } \Omega_l, \quad (1a)$$

$$\nabla \cdot \mathbf{u} = 0 \quad \text{in } \Omega_l, \quad (1b)$$

where \mathbf{u} is the velocity vector, p the pressure, ρ the constant blood density, ν the constant kinematic viscosity and $\mu = \rho\nu$ the constant dynamical viscosity.

The hemodynamics is characterized by the Reynolds number $Re = (2Q_v) / (\pi R_1 \nu)$ based on the volumic blood flow rate Q_v and the luminal radius R_1 . As in Jansen et al. [12], we choose $Re_0 = 300$ at t_0 , and the initial luminal domain is a straight artery of uniform radius R_0 and of length $L = 45R_0$. Throughout the IH lesion development, we assume axisymmetric morphological changes of Ω_l , so that hemodynamical variables (\mathbf{u}, p) are only radially- and axially-dependent. Three-dimensional hemodynamically simulations are therefore done in a wedge geometry, which is used to solve equations in the azimuthal plane, assuming axisymmetry of the problem.

The boundary conditions (BCs) applied at each surface of the luminal domain are

$$\text{at } \Gamma_1^{\text{in}} : \begin{cases} \mathbf{u} = u_{\text{max}} (1 - (y/R_{1,\text{in}})^2) \mathbf{z}, \\ \nabla p \cdot \mathbf{n} = 0, \end{cases} \quad (2a)$$

$$\text{at } \Gamma_1^{\text{out}} : \begin{cases} (\nabla \mathbf{u}) \cdot \mathbf{n} = \mathbf{0}, \\ p = 0, \end{cases} \quad (2b)$$

$$\text{at } \Gamma_1^{\text{e}} : \begin{cases} \mathbf{u} = \mathbf{0}, \\ \nabla p \cdot \mathbf{n} = 0, \end{cases} \quad (2c)$$

$$\text{at } \Gamma_1^{\text{w}0,1} : \begin{cases} (\nabla \mathbf{u}) \cdot \mathbf{n} = \mathbf{0}, \\ \nabla p \cdot \mathbf{n} = 0, \end{cases} \quad (2d)$$

with spatial domains specified in Figure 1. \mathbf{n} is the unit normal vector and is $R_{1,\text{in}}$ the inlet luminal radius. At inlet, the velocity is prescribed as Poiseuille parabolic velocity profile (2a) assuming fully developed blood flow upstream the inlet. For consistency with the imposed velocity field, we assign zero pressure gradient at inlet. At outlet (2b), zero gradient is imposed for the velocity field and pressure is set to 0, so that the resolved pressure field corresponds to pressure *variations* about this reference value. At the endothelium surface (2c), a no-slip condition is assumed, *i.e.* zero velocity relative to the wall which is assumed rigid in hemodynamical timescale [12]. Finally, zero pressure gradient is imposed at wall.

The wall shear stress (WSS) vector is $\boldsymbol{\tau}_w$ and of magnitude τ_w :

$$\boldsymbol{\tau}_w = \mu (\boldsymbol{\nabla} \mathbf{u} + \boldsymbol{\nabla} \mathbf{u}^T) \cdot \mathbf{n} \quad \text{in } \Omega_e, \quad (3a)$$

$$\tau_w = |\boldsymbol{\tau}_w| \quad \text{in } \Omega_e. \quad (3b)$$

It represents the tangential friction stress exercised by blood on the luminal wall. (3b) is used in the present model to account for hemodynamics in the IH model.

CFD computations use the **OpenFOAM** code version 5.0 [19], a C++ object oriented library widely used in research and industry. It is open source, efficient, flexible, and easily updatable. **OpenFOAM** implements the Finite Volume Method (FVM) on cartesian and collocated grids.

Under axisymmetric assumption, the computational luminal domain is a thin wedge of angle θ and of one cell thick along the circumferential direction [19] (shown in left Figure 1).

We use the Semi-Implicit Method for Pressure-Linked Equations (SIMPLE) solver proposed by default in **OpenFOAM** [19] to solve equations (1) with boundary conditions (2). The parameters chosen for our **OpenFOAM** simulations are listed in Table 1 for boundary conditions and Table 2 for Navier–Stokes equations discretization.

For the first hemodynamical generation in the geometry of Figure 1, we initialize velocity and pressure fields as a Poiseuille flow. The initial guess velocity profile is in equation (2a) and initial pressure field is $p(z) = -Gz + p_{\text{in}}$, with $G = -(p_{\text{out}} - p_{\text{in}})/L$ the pressure gradient and L the total length of the artery.

The 3D wedge mesh is built using **Gmsh** [9]. It is a structured mesh composed of prisms along the axis of symmetry of revolution and hexahedral elements with non-uniform grading in radial direction, as well as at inlet and outlet. The cells are also denser near wall for accurate evaluation of the WSS. Numerical data for the luminal mesh discretization are provided in Table 3 and an illustration of the mesh construction is shown in Figure 14 (d). Luminal mesh parameters for the results presented hereafter are chosen after a mesh convergence study (see appendix B).

2.2 Intimal hyperplasia modelling

The multiscale compartmental model of IH presented in [12] describes the kinetic of vascular species in layers of a spatial domain called compartment. It considers cellular populations as vascular smooth muscle cells (vSMCs) — through their phenotypical state, contractile (cSMCs) and secretory (sSMCs) — endothelial cells (ECs), and non cellular population as young and old

collagen fibers. The model contains biochemical equations for growth factors (GFs) dynamics, organized in seven families.

In this paper, we apply our modelling of IH development on an axisymmetric idealized artery. This section is a brief presentation of the model in this novel geometrical configuration.

Each compartment of arterial volume is labeled with upper index, as are all variables localized in this compartment. The kinetic differential equations of our model have the same structure: they express the rate of variation in time of a variable denoted by index “i” as X_i^j in the compartment “j”. This rate of variation is set by the sum of the functional properties (FPs). Each variable is either a species count or a growth factor amount. The generic form of model equation is therefore

$$\frac{dX_i^j}{dt} = M_i^j + f_i^0 X_i^j - f_i^1 X_i^j + \text{cp}^j \quad \text{in } \Omega_i^j \quad (4)$$

where M_i^j is a source term, f_i^0 and f_i^1 are two FPs — *e.g.* proliferation and apoptosis — cp^j are the coupling terms with other variables, and Ω_i^j is the spatial domain. For the j^{th} compartment, the set of differential equations of the model can be written in vectorial form as

$$\frac{d\mathbf{y}^j}{dt} = \mathbf{f}(\mathbf{y}^j, \mathbf{y}^j(t - \tau_C), \tau_w^j), \quad (5)$$

where \mathbf{y}^j is the vector of variables composed of species and GFs, t is the time, $\mathbf{y}^j(t - \tau_C)$ is the vector of variables evaluated at time $t - \tau_C$ with τ_C the collagen ageing delay, τ_w^j is the magnitude of WSS and \mathbf{f} the right-hand-side vector function. Equations (5) is solved numerically for each compartment over a timespan between t_0 and t_f with an initial condition $\mathbf{y}^j(t_0) = \mathbf{y}_0^j$ and a given history $\mathbf{y}^j(t) = \mathbf{h}^j(t)$ for $t_0 - \tau_C \leq t < t_0$. The resolution of the system (5) is done with a Runge–Kutta solver based on [17]. For better comparison of tri-dimensional model results with the one-dimensional test-case [12], we retain identical constants of the models, initial condition and history. See Jansen et al. [12] for a detailed description of the model, including species functional properties (SFPs) integrated, constant parameters, initial and historical conditions and numerical time-marching algorithm.

As mentioned, we apply here the IH model to the case of an axisymmetric idealized artery, using a tridimensional formulation. Keeping the compartmental approach, we consider an arterial wall mesh composed of N_{TG} compartments, in which we apply the set of equations (5). Figure 1 (Right) shows an illustration of the arterial wall mesh and the compartmental configuration, in which there is an absence of coupling between

neighbouring compartments. Thus, the spatial dependences are implicit in (a) longitudinal direction due to the coupling with the local hemodynamical WSS and (b) radial direction by the use of modelled intima and media layers of a compartment. The assumption of decoupled neighbouring compartments results in the neglect of phenomena applying in the longitudinal direction, such as molecular diffusion of GFs or cellular migration, which tend to spread out matter and, generally, homogenize it in space. Unfortunately, as we neglect these phenomena, we may produce, from this compartmental modelling, significant variability of tissue dynamics between several neighbouring compartments. So-called “non-biophysical gradient of dynamics” may arise within the compartmental arterial wall mesh, especially if the hemodynamical WSS, a derived variable of a CFD computation, is coarsely solved numerically. Macroscopically, non-biophysical gradients may thus produce stiff morphological changes of the artery which, over hemodynamical generations, can lead to a divergence of the simulation due to under-resolution of the mesh deformation. This imposes a fine discretization in zones of biophysical gradients. A mesh convergence study, presented in Appendix B, has permitted to set adequate values of N_{TG} and CFD mesh parameters.

Moreover, one can model threshold phenomena with the piecewise-defined Macaulay function noted $\langle \cdot \rangle$, for migration and dedifferentiation on vSMCs [12]. This may produce the arising of non-biophysical gradients in some regions. To avoid this, we introduce a modified Macaulay function (MMF), noted $\langle \cdot \rangle^*$, which is smoother than $\langle \cdot \rangle$. The MMF is

$$\langle x - x_0 \rangle^* = \begin{cases} \frac{(x - (x_0 + l_M))^2}{4l_M}, & \text{if } x \in [x_0 - l_M, x_0 + l_M], \\ \langle x - x_0 \rangle, & \text{otherwise,} \end{cases} \quad (6)$$

with x_0 a threshold value and l_M the half smoothing distance. In the present study, this MMF function replaces the Macaulay function in the SFPs, *i.e.* migration and dedifferentiation of vSMCs.

2.3 Coupling methods in a bidimensional domain

The coupling methods introduced in [12] are suitable for 2D axisymmetric configuration. The coupling between hemodynamics/biochemistry and biochemistry/SFPs is the same as in the monodimensional case, except that WSS stimuli are now distributed over the length of the artery. The WSS stimulating each compartment is the magnitude τ_w of the WSS vector from CFD (equation (3b)), interpolated using cubic spline at each endothelium face centre of compartments. This allows to con-

sider non-conforming meshes between luminal and parietal meshes, *i.e.* non-coincidence of vertices of the two domain meshes at the endothelial surface.

A specific strategy is developed for the coupling between hemodynamics and arterial wall remodelling. From a separation of timescales of tissues growth and hemodynamics and as in other studies [1, 6, 5], we continue to assume loose coupling between arterial tissue dynamics and hemodynamics under the inward-hypertrophic remodelling hypotheses [12]. As in our previous study, remodelling of the whole luminal mesh domain occurs if either of the following conditions is reached on any compartment

$$\frac{V_{\text{all}}^j - V_w^j}{V_1^j} > 1 + \varepsilon, \quad (7a)$$

$$\frac{V_{\text{all}}^j - V_w^j}{V_1^j} < 1 - \varepsilon. \quad (7b)$$

ε is a remodelling parameter indicating hemodynamics sensitivity to tissues growth. V_{all}^j is the j^{th} whole constant arterial volume, calculated as $V_{\text{all}}^j = \Delta z^j \pi (R_{\text{ext}}^j)^2$ with Δz^j and R_{ext}^j respectively the length of the compartment and the external radius of the j^{th} compartment. V_w^j is the j^{th} time-dependent arterial wall volume defined from species dynamic evolution (see [12, eq. 12c] for definition). V_1^j is the j^{th} morphological-generation-dependent luminal volume calculated as $V_1^j = \Delta z^j \pi (R_1^j)^2$ where R_1^j is the luminal radius of the j^{th} compartment associated with the current hemodynamical generation. As soon as a remodelling is detected from the conditions (7), all the luminal volumes V_1^j are updated in accordance with the new arterial morphology. Considering criterions (7), we compute for each compartment the ratio of the luminal volume at tissue growth timescale $V_{\text{all}} - V_w$ over the luminal volume at hemodynamic timescale V_1 . More precisely, (7a) corresponds to a tissue loss with an enlargement of the lumen, and (7b) corresponds to a tissue growth with luminal narrowing. Both criteria (7) are defined as terminal events, *i.e.* terminate the time integration when an event occurs and modify the set of equations before a possible restart. The method of automatic detection of hemodynamical remodelling is a novelty compared to previous studies [6, 1, 5] which consider constant intervals between two consecutive remodellings.

In monodimensional domain, the update of the morphology of an artery is trivial as we consider a unique compartment. Considering higher dimension, after arterial wall discretization into compartments, we integrate N_{TG} times the system of equations (5). Related to the spatially-dependent dynamics of intimal hyperplasia, induced by WSS distributions and/or initial conditions,

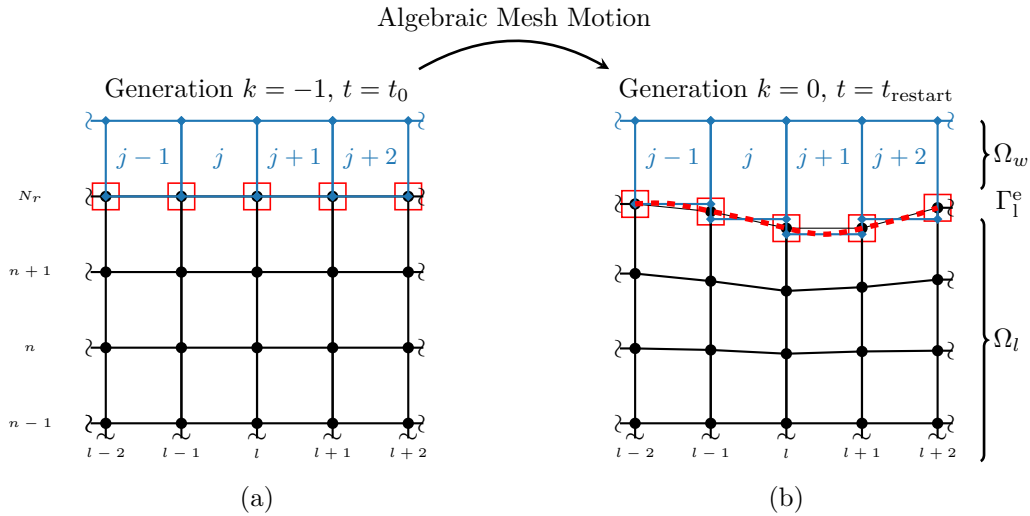


Fig. 2: Algebraic mesh motion strategy between two luminal meshes with (a) a first straight initial generation $k = -1$ and (b) a second deformed generation $k = 0$ at restart time t_{restart} . Part of luminal mesh (solid line with circular vertices) and parietal mesh (solid line with diamond vertices and compartment labeled with index j) are illustrated on both sides of the endothelium surface Γ_1^e at the interface between luminal domain Ω_l and parietal domain Ω_w . l and n are respectively increment in the longitudinal and radial direction labeling vertices in meshes. Cubic spline interpolation (dashed line in (b)) of luminal radius of compartments at $t = t_{\text{restart}}$ permit to evaluate new luminal vertices at Γ_1^e noted $R_1^{l, Nr}$ (surrounded with square). Using the algebraic mesh motion relation (9), all the vertices of the luminal mesh are moved as seen in (b).

any compartment can reach criteria (7). The strategy to handle correctly the update between two successive arterial generations is explained in the following, for the first arterial generation.

From N_{TG} initial conditions and histories at $t = t_0$, the time-marching algorithm starts until the desired final time $t = t_f$. If compartments experiment one of the terminal remodelling criteria (7), one has to locate the minimum instant from all compartments. This instant is the next restart time for the new time integration of (5) for all compartments of the parietal mesh, noted t_{restart} , and it is defined as

$$t_{\text{restart}} = \min_{\forall j} (t_f^j), \quad (8)$$

with t_f^j the final time of the j^{th} compartment. Once the restart time is known, we evaluate all the luminal radius of compartments along the artery at time $t = t_{\text{restart}}$ to calculate the arterial morphology of the next morphological generation : $R_{k+1}(z) = R^j(t_{\text{restart}})$. Using R_{k+1} , we apply a mesh motion on the luminal mesh to generate the next one.

Considering axisymmetric luminal morphological changes, we can manage mesh motion with a simple algebraic expression assuming only radial mesh vertices displacement while retaining good mesh properties over morphological changes, such as mesh non-orthogonality

and skewness. An illustration of a CFD mesh motion is given in Figure 2 where discrete compartmental radius R^j and the morphological changes $R_1(z) = R(t_{\text{restart}})$ are represented. A cubic spline interpolation is used to evaluate luminal radius from the centre of compartments to the vertices of the boundary surface Γ_1^e , noted $R_1^{l, Nr}$ (see Figure 2). Considering the mesh motion for the generation $k + 1$, the algebraic relation for radial coordinate of the mesh vertices, noted $r_{k+1}^{l, n}$, read

$$r_{k+1}^{l, n} = r_0^{l, n} E_{k+1}^l \quad (9)$$

with l and n respectively the longitudinal and the radial increment, $r_0^{l, n}$ radial position of initial mesh generation and $E_{k+1}^l = R_{k+1}^{l, Nr} / R_0$ the radial deformation from initial configuration.

Once the mesh is updated thanks to equation (9), a next cycle starts as: computing a new CFD simulation according to the novel arterial morphology and luminal mesh, then updating the set of equations (5) based on a new WSS distribution, and finally, restarting the time integration of IH model until reaching t_f or detecting a new remodelling criteria and starting again the whole procedure.

Another situation is the return to an equilibrium state of the entire wall during the resorption of the pathology, or when a new equilibrium is reached as in our test-case [12]. We add, to the terminal remodelling

criteria, a non-terminal stopping criterion and suppose that the arterial wall return to equilibrium if all compartments check

$$\left\| \left[\frac{d\mathbf{y}^\dagger}{dt^\dagger} \right]^j \right\| < \epsilon, \quad (10)$$

where ϵ is the equilibrium sensitivity parameter, $\|\cdot\|$ the L_2 norm and $\left[\frac{d\mathbf{y}^\dagger}{dt^\dagger} \right]^j$ the dimensionless time derivative \mathbf{y} of the j^{th} compartment (see [12] for the definitions of dimensionless variables).

2.4 Disendothelization models

Considering the same approach as in our validation test-case [12], we investigate the response of the artery to mechanically-induced local damages. A localized damage of the endothelial cell (EC) layer disturbs the homeostatic equilibrium of our model and it initiates a tissue growth response, already described in [12].

These damages are imposed as initial conditions for the equations governing the evolution of ECs. They are limited to a defined region in the longitudinal direction in $z \in [z_l, z_u]$ with z_l and z_u respectively the lower and upper longitudinal limits of the damages.

Firstly, we consider, using hyperbolic tangent functions, a so-called bump damage (BD) of the form

$$E_0^\dagger(z) = 1 + \frac{1 - d_0}{2} \left[\tanh \left(-\frac{z - z_l^{\text{BD}}}{\delta_z} \right) + \tanh \left(\frac{z - z_u^{\text{BD}}}{\delta_z} \right) \right], \quad (11a)$$

with E^\dagger the ECs count E divided by its maximal value E_{max} , δ_z parameter to adjust the length of transition zone between healthy and damaged zone, d_0 initial damage parameter and $z_{u,l}^{\text{BD}}$ limits of the damaged zone.

Another gaussian damage (GD) is applied, using gaussian function, as

$$E_0^\dagger(z) = 1 - d_0 \exp \left(-\frac{(z - z_G)^2}{2\sigma_G^2} \right), \quad (12)$$

with z_G centre of the damaged zone and σ_G the damage length control parameter. Lower and upper limits of GD are respectively defined as $z_l^{\text{GD}} = x_G - 1.18\sigma_G$ and $z_u^{\text{GD}} = x_G + 1.18\sigma_G$ so that for both damages we get $E_0^\dagger(z_{u,l}) = 0.5$.

Figure 3 presents the two analytical damage functions chosen in equations (11) and (12). In a region of equivalent length, the considered damages model the following two types of disendothelization as

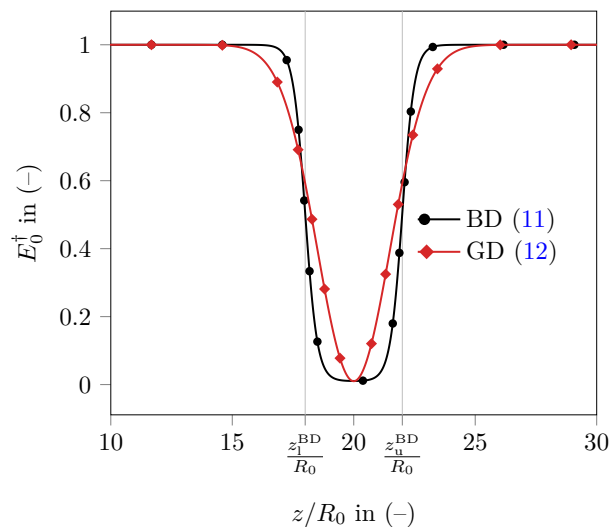


Fig. 3: Gaussian (diamond symbols) and bump (circle symbols) damages applied to the endothelium at initial time. x -axis is the dimensionless longitudinal position z/R_0 and y -axis is the initial value of $E_0^\dagger = E_0/E_{\text{max}}$ the rescaled endothelial cells population with E the ECs count and E_{max} the maximal value.

- a focal damage, where endothelium is strongly injured on the major part of the damage zone and where transition between healthy and damaged zone is stiff;
- a diffuse damage, where the disendothelization is severe on a small zone with smooth transition between healthy and damaged zone.

The comparison of two different initial damages aims to quantify the influence of initial conditions on the lesion developments predicted by our model of IH in an axisymmetric artery at $Re_0 = 300$.

3 Results and Discussions

First, we present in section 3.1 the macroscopic spatio-temporal evolution of lesions with: in section 3.1.1, an analysis of remodelling dynamics via the detection of criteria (7); in section 3.1.2, a discussion on the dynamics of the luminal radius in both damages; in section 3.1.3, a comparison of mono- and bi-dimensional results in terms of luminal radius and WSS to discuss the main differences between cases; in section 3.1.4, an evaluation of the mesh motion procedure as well as CFDs resolutions.

Finally, we consider microscopic scales in section 3.2. The macroscopic dynamics is induced by the species dynamics, that we present in the following sections: 3.2.1, presenting the ECs regenerations; 3.2.2, discussing

the various functional properties of vSMCs; 3.2.3, discussing the dynamics of sSMCs populations within intima and media layers and 3.2.4, presenting the composition of intimal layer during the development of the lesions.

3.1 Macroscopic lesion evolution

3.1.1 Detection of remodelling criteria

Firstly, we present the spatio-temporal evolution of the detection of criteria (7) inducing hemodynamical remodelling. As this type of automatic remodeling has never been implemented to our knowledge, we present in detail the detections of remodeling events which have a non-trivial behavior. Figure 4 shows the instants where hemodynamical remodellings are performed, for gaussian and bump damages. For each data point in this figure, a terminal event from criteria (7) has been located. Depending on the remodelling times, we report the associated dimensionless longitudinal position within the artery of the compartment which experimented this event, noted z_c/R_0 , along with its dimensionless radius R_c/R_0 . This figure gives an overview of the dynamics of lesions through the evolutions of events detection. Reading this graph helps to locate longitudinal zones and time intervals of interest in the lesion developments.

Between 0 and 10 days, both damages exhibit the same evolution of the detection of events spatially and temporally. The hotspots of tissues growth are localized at the centre of the damaged zones ($z/R_0 \sim 20$) and the compartmental radius R_c decrease is the same. During the first ten days, hotspots of tissues growth move slightly downstream of the initial maximal damaged point at $z/R_0 = 20$.

From day 10, GD and BD cases stop having the same behaviour. The GD compartmental radius R_c^{GD} decrease slows down and reaches its minimal radius ($R_c^{\text{GD}} = 0.91R_0$) on day 19 and at longitudinal position $z_c^{\text{GD}} = 20.4R_0$. However, the BD compartmental radius R_c^{BD} still decreases until reaching a first minimal radius ($R_c^{\text{BD}} = 0.89R_0$) on day 17.6 at longitudinal position $z_c^{\text{BD}} = 20.8R_0$. During these two luminal radius decrease phases, the detected events are all of the narrowing type (7b).

The two dynamics of criteria detection diverge around day 20. We begin with the discussion of GD lesion evolution, before that of the BD lesion in the next paragraph.

For the GD case, there is a breakpoint in the lesion dynamics at day 21.5 materialized by the detection of a first enlargement criterion (7a) at longitudinal position $z_c^{\text{GD}} = 20.1R_0$. This new type of event detected

produces a gap in z_c/R_0 evolution (shown with vertical lines in Figure 4). This reflects the fact that, after approximately 20 days in the zone initially damaged, there is a stronger resorption of the lesion in the initial damaged zone than a tissue growth occurring downstream of $z/R_0 = 20$ (see Figure 5). This lesion resorption has been presented in our previous work [12] and will be discussed in section 3.2 at the cellular scale. For $t \in [21.5, 46.4]$ days, only enlargement criteria are detected in GD. At $t = 47.7$ days, another gap in z_c^{GD}/R_0 evolution is seen. It points out the detection of narrowing events (7b) localized downstream the initial damaged zone ($z_c^{\text{GD}} = 22.2R_0$). Finally, a last switch from narrowing to enlargement criterion is seen on day 65.6. Until $t = 100$ days, the GD compartmental radius R_c^{GD} grows slowly.

For the BD lesion, the first switch from narrowing to enlargement events is seen after that of GD on day 24 at longitudinal position $z_c^{\text{BD}} = 20.2R_0$. Between this instant and until day 35.3, only enlargement events are detected and the luminal radius R_c^{BD} increases. From day 35.3 to day 57.2, the last switch of type of event, the lesion gets into another growing phase downstream the damaged zone. The BD lesion reaches the minimum compartmental luminal radius at event instants ($R_c = 0.87R_0$) at $t = 51.3$ days at the longitudinal position $z_c^{\text{BD}}/R_0 \sim 22.5$. Finally from day 57.5 until $t = 100$ days, events detected are all of the enlargement type (7a) and R_c^{BD} grows slowly as for GD lesion.

In summary, the number of events detected after 100 simulated days for GD and BD lesion are respectively 110 and 249 for as many CFDs carried out. On day 100, the BD case causes about twice as many remodelling as the GD case, whereas at $t \sim 40$ days the number of criteria detected for the GD and BD cases are respectively 63 and 86. This important difference, in terms of number of remodelling between the two cases, is due to the important phase of tissue growth downstream of the initial damage in the BD lesion (see Figure 5). Thus, the lesion dynamics downstream of the initial injury, induced by the dynamics of the underlying vascular species, in the BD case is exacerbated compared to the GD case. We will discuss the phases of narrowing observed downstream of the initial damages seen in Figure 4, for the BD between $z_c^{\text{BD}}/R_0 \in [22, 22.7]$ and for the GD between $z_c^{\text{EG}}/R_0 \in [22.2, 22.5]$, in section 3.2 by presenting the dynamics of vascular species in these zones.

The minimum time interval between two successive hemodynamical generations is for the GD and BD cases respectively of 0.38 days ($\sim 3.2892 \times 10^4$ seconds) and 0.227 days ($\sim 1.9613 \times 10^4$ seconds). This result supports our hypothesis of timescale separation between

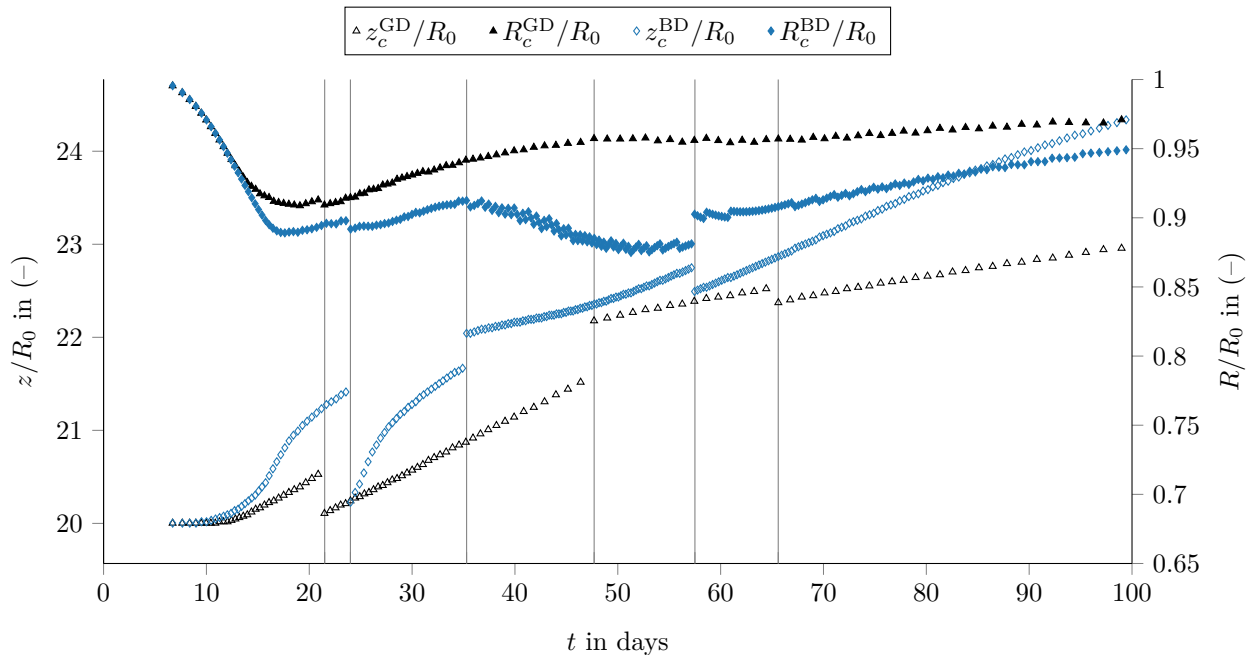


Fig. 4: Instants of narrowing and enlargement events detected during the gaussian (GD) and bump (BD) damages. Left y -axis: Longitudinal position normalized by the initial radius z/R_0 . Right y -axis: Luminal radius normalized by R/R_0 at the instant of detection. Vertical lines highlight the switch from one type of event detected to another.

tissue growth and hemodynamics, which assumes a succession of quasi-static states over the course of pathological development.

3.1.2 Evolution of the luminal radius

We discuss the spatio-temporal evolutions of the luminal radius of arteries in the pseudo-color plots in Figures 5 (a,b). Throughout this article, plots of this type are obtained from Gouraud (bi-linear) interpolation of the data from the simulations of the model on the compartmental mesh of the arterial wall. Figures 5 (a,b) allow the overall visualization of the onset of lesions and displacements downstream of the damaged zones. In addition, snapshot of luminal morphologies over several instants permit a quantitative comparison between the two types of initial damages in Figures 5 (c,d).

Regarding Figures 5 (a) and (b), and as already described with event detections in section 3.1.1, we observe between 0 and 20 the lesion onset in the damaged zones for both cases. After 20 days, the lesions develop downstream from the initial injury, strongly for the BD lesion that reached the longitudinal position $z \sim 24.1R_0$ at day 100, and to a lesser extent for the GD lesion reaching $z \sim 22.9R_0$ at day 100. In both cases, this displacement is explained by the WSS distribution downstream the incipient lesion between 0 and

20 days (see Figures 8 and 9) which induces a prone zone to hyperplasia (see Figure 12).

We compare the maximum predicted stenoses in the two simulations. In GD case, the maximal lesion ($R_1 = 3.56$ mm) is observed at $t = 20.9$ days at $z \sim 20.3R_0$. From there, the lesion decreases as it continuously moves downstream. On the contrary, the maximal lesion in the BD case ($R_1 = 3.439$ mm) is observed at $t = 54.1$ days at $z \sim 22.5R_0$. Furthermore, we also observe in BD a growth of the same intensity ($R_1(t = 20\text{d}, z \sim 20.5R_0) = 3.453$ mm) at day 20 around the centre of the artery (see Figure 5 (d)). This highlights the main difference between the two models of damage: the BD lesion meets another important tissue growth phase during its downstream movement. Thus, the downstream zones of stenosis may be more prone to tissue growth induced by wall shear stress values, than the initially damaged zone where tissue growth is provoked by a disturbance of the homeostatic equilibrium.

The difference of spatio-temporal evolution of $R_1(t, z)$ is mainly due to the morphological differences of the lesions at short time which drive the longitudinal variation of WSS (see Figure 8). In GD case, the stenosis is smoother than in the BD case (see Figures 5 (c) and (d) at $t = 30, 40, 50$ days). These morphological differences induce lower WSS downstream of the lesion for

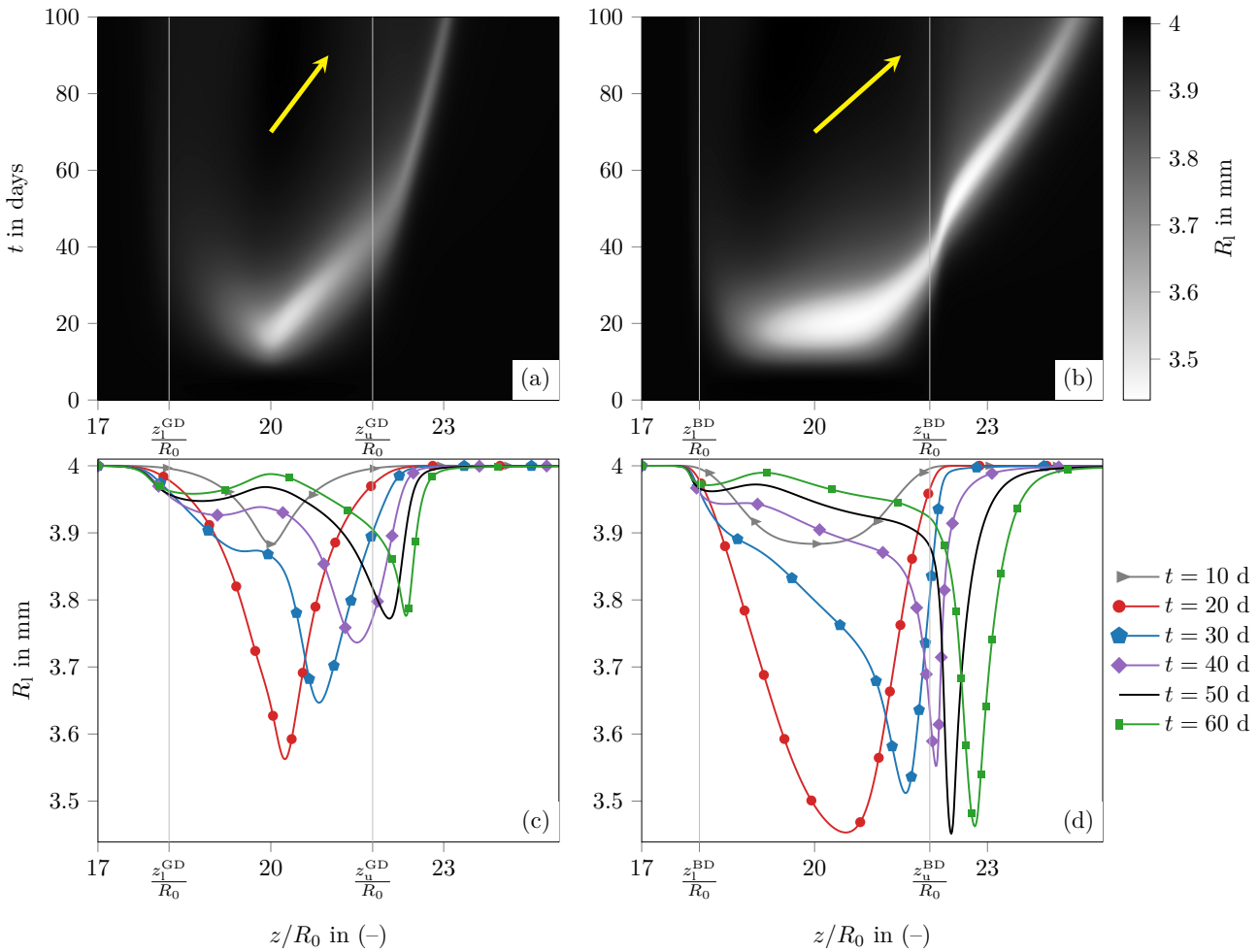


Fig. 5: Spatio-temporal evolution of the luminal radius $R_1(t, z)$ for gaussian (a) and bump (b) damages. x -axis is the dimensionless longitudinal position z/R_0 . For (a) and (b), y -axis is time in day. Arrows show the displacement of lesions downstream of the initial damaged zones. Snapshots of $R_1(t, z)$ at 10, 20, 30, 40, 50 and 60 days are drawn in GD (c) and BD (d) cases.

the BD case as shown in Figure 8 from $t > 15$ days. Our model associated with the BD case therefore predicts an important growth phase not induced by the injury but by the distribution of WSS, which goes in the direction of the macroscopic hypotheses on the importance of pathology-promoting zones with “disturbed flow” [20, 15]. This result is built only from biochemical and cellular hypotheses proposed in [12]. We describe in section 3.2 the dynamics of vascular species inducing tissue growth in zones of low WSS.

As soon as the lesion begins to move downstream, this initiates self-maintenance of this displacement. Indeed, downstream of a developing stenosis, a new pathology-promoting zone will appear because of low WSS values. We refer the reader to Figure 9 showing the evolution of the minimum of WSS over the time and the longitudinal position. These distributions of WSS

explain the continuous downstream movement of the lesion which is indicated by arrows in Figure 5 (a) and (b).

3.1.3 Comparison between 1D and 2D geometries

At the centre of the two damaged zones ($z/R_0 = 20$), we compare in Figure 6 axisymmetric and monodimensional results through the temporal evolution of luminal radius and WSS.

Figure 6 (a) presents the evolution of WSS between 0 and 100 days in 1D and axisymmetric cases. We observe the same global dynamics of WSS dictated by the phases of lumen narrowing and enlargement, respectively inducing the phase of increase and decrease of WSS. However, these phases have neither the same timescales nor the same amplitudes. We explain these

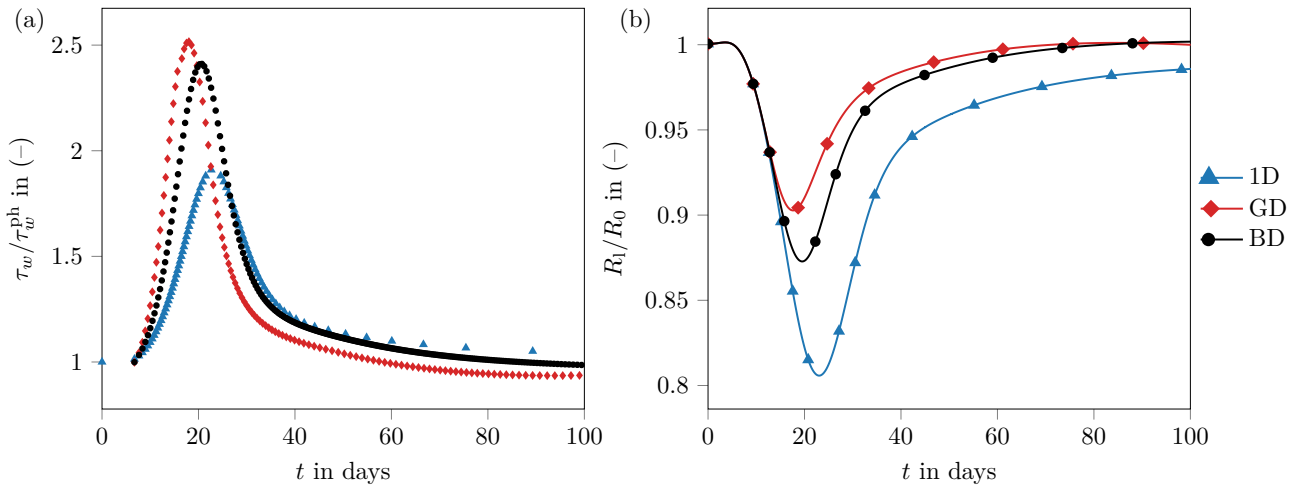


Fig. 6: Comparison between 1D case-test [12] (triangle symbols), GD (diamond symbols) and BD (circle symbols) cases at the compartment localized at $z/R_0 = 20$ between 0 and 100 days. (a) WSS normalized by the physiological value $\tau_w/\tau_w^{\text{ph}}$ along the arterial generations. (b) Normalized luminal radius R_1/R_0 as function of time.

differences because in the 1D case, we assume an infinitely pathological artery without taking into account the converging and diverging zones of the blood flow upstream and downstream of the stenosis resulting from the tissue growth. These zones of flow acceleration and deceleration, on either side of the lesion, produce this WSS-observed increase in the axisymmetric configuration.

We also observe a deviation of the duration of the growth phase of WSS between mono- and bidimensional configuration, *i.e.* in GD $\tau = 18$ days, in BD $\tau = 20.7$ days and in 1D case $\tau = 22.6$ days. These timescale deviations from 1D test-case, are due to the differences in the intensities of the WSS. Indeed, when the arterial wall is subjected to a WSS higher than the physiological-initial value, our model promotes lesion resorption to the detriment of tissue growth due to the bioavailability of growth factors. The higher the WSS, the greater the biochemical state of protection against tissue growth and the shorter the phase of tissue growth, *e.g.* with the minimum phase of growth ($\tau = 18$ days) for the maximum values of WSS. Thus, this contraction of the duration of tissue growth is maximum in the GD case, compared to the other cases, because the WSSs in this case are higher.

Figure 6 (b) compares the evolution of the luminal radius for the three cases. As for the dynamics of the WSS, R_1/R_0 follows the same phasic evolution with tissue growth followed by tissue loss. In bidimensional cases, the lesions are less severe than the 1D case, although they are induced by the same initial disendothelization ($E^\dagger(t_0, z = 20R_0) = 1 - d_0$). It is mainly due to the higher WSS discussed below. It emerges

from this comparison that the hypothesis of monodimensional configuration, *i.e.* an infinitely long damage, posed to test our model in a simple one-dimensional configuration, has a strong importance on lesion development at $z/R_0 = 20$ especially at short time.

3.1.4 Arterial generations: CFD resolutions and wall shear stress stimuli

In Figure 7 (a), by plotting the maximum of the faces non-orthogonality parameter $\theta_{\text{face}}^{\text{max}}$ returned by the `checkMesh` utility of `OpenFOAM`, we assess the quality of CFD meshes in GD and BD cases of all the arterial generations created from the moving mesh strategy introduced in section 2.3. As supposed, the variations of $\theta_{\text{face}}^{\text{max}}$ in the GD case (maximum of 12.74° at the 85th generation) are limited compared to the BD case which predicts stiffer luminal morphologies (see Figure 5 (d)). The $\theta_{\text{face}}^{\text{max}}$ parameter in BD increase until a maximum (35.57° at the 92th generation) then decreases as tissue growth loses intensity (see Figure 5).

To illustrate a mesh obtained by the algebraic mesh motion algorithm in the period where $\theta_{\text{face}}^{\text{max}} > 30^\circ$, we propose a `ParaView` visualization in Figure 7 (c) of 84th arterial generation at $t = 39.9$ days. The mesh, visible in black lines, is coloured by the non-orthogonality of cells field $\theta_{\text{cell}}^{\text{max}}$. The maximum non-orthogonality is localized downstream of the stenosis and near the wall, in the zone where the variations in the luminal radius are stiffer. According to the maximum value of $\theta_{\text{face}}^{\text{max}}$ in Figure 7 (a) and the general appearance of a stiff arterial morphology mesh in Figure 7 (c), we can validate

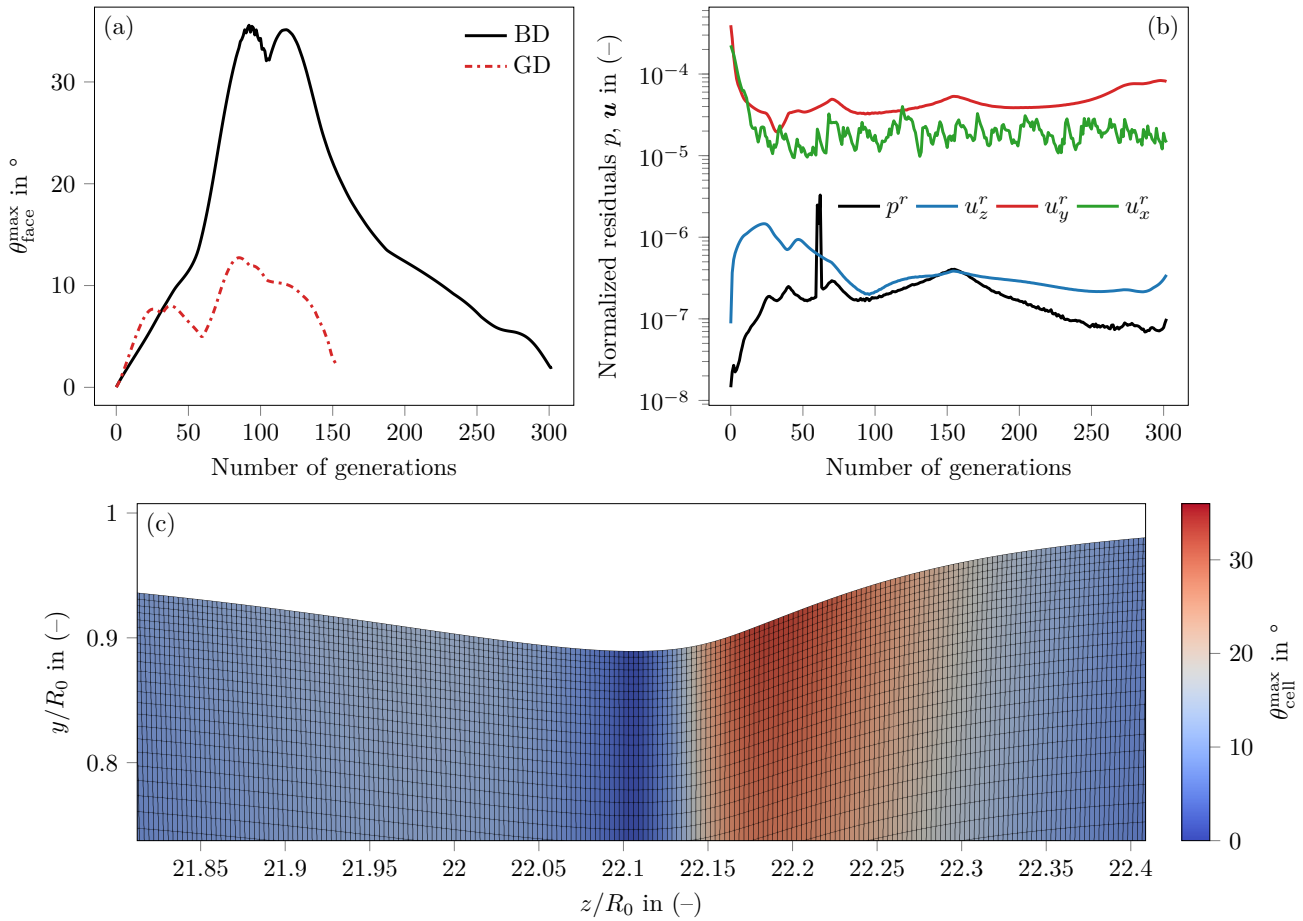


Fig. 7: (a) Maximum face non-orthogonality parameter $\theta_{\text{face}}^{\text{max}}$ as a function of the generated luminal meshes (number of arterial generations calculated) in gaussian damage (dashed lines) and bump damage (solid lines). (b) Normalized residuals of pressure and velocity at the last SIMPLE iteration as a function of arterial generations in BD case. (c) ParaView mesh visualization of the 84th arterial generation at $t = 39.9$ days in the stenosis zone of the BD case. In pseudo-colors, the cell non-orthogonality parameter field $\theta_{\text{cell}}^{\text{max}}$ is presented.

the proposed algebraic mesh motion strategy in the two types of damage considered here.

We now study the convergence of hemodynamics simulations during the pathological development in the BD case. In Figure 7 (b), we plot, as a function of arterial generations, the final pressure and velocity normalized residuals of the SIMPLE algorithm. The values of the residues reported are those of the final state of the numerical resolution at each arterial generation and not a continuous variation of residuals. This plot shows that all the hemodynamics simulations are sufficiently converged. The maximum normalized residuals for all generations are respectively $p_{\text{max}}^r = 3.29 \times 10^{-6}$, $u_{z\text{max}}^r = 1.46 \times 10^{-6}$, $u_{y\text{max}}^r = 3.96 \times 10^{-4}$, $u_{x\text{max}}^r = 2.25 \times 10^{-4}$.

Finally, to conclude on the macroscopic variables, the spatio-temporal variations of WSS are presented. We show in Figure 8 the spatial variations of WSS over

several arterial generations in GD and BD cases. Since the two damage models present different lesion dynamics, there is no arterial generation having in common the same instant of remodelling in GD and BD. However, wishing to compare the WSS at equivalent times in both cases, we present in Figure 8 the hemodynamic generations having similar remodelling instants. These moments of generations — denoted by $t_{k_{\text{GD}}, k_{\text{BD}}}$ with k_{GD} and k_{BD} respectively the generational indexes of GD and BD cases — are respectively $t_{-1, -1} = 0$ d, $t_{6, 6} = 10.0$ d, $t_{17, 18} = 14.8$ d, $t_{28, 32} = 20.3$ d, $t_{36, 41} = 24.9$ d, $t_{48, 55} = 30.0$ d, $t_{57, 69} = 35.2$ d et $t_{63, 83} = 39.9$ d.

As already compared at $z/R_0 = 20$ (see Figure 6), at short timescale in the strongly damaged zone, the WSS of the GD case is higher than that of the BD case. Quickly, from $t = 20$ days, the maximum of WSS in both cases move downstream of the initial damaged zone. In the meantime, a zone of low WSS ($\tau_w/\tau_w^{\text{ph}} < 1$)

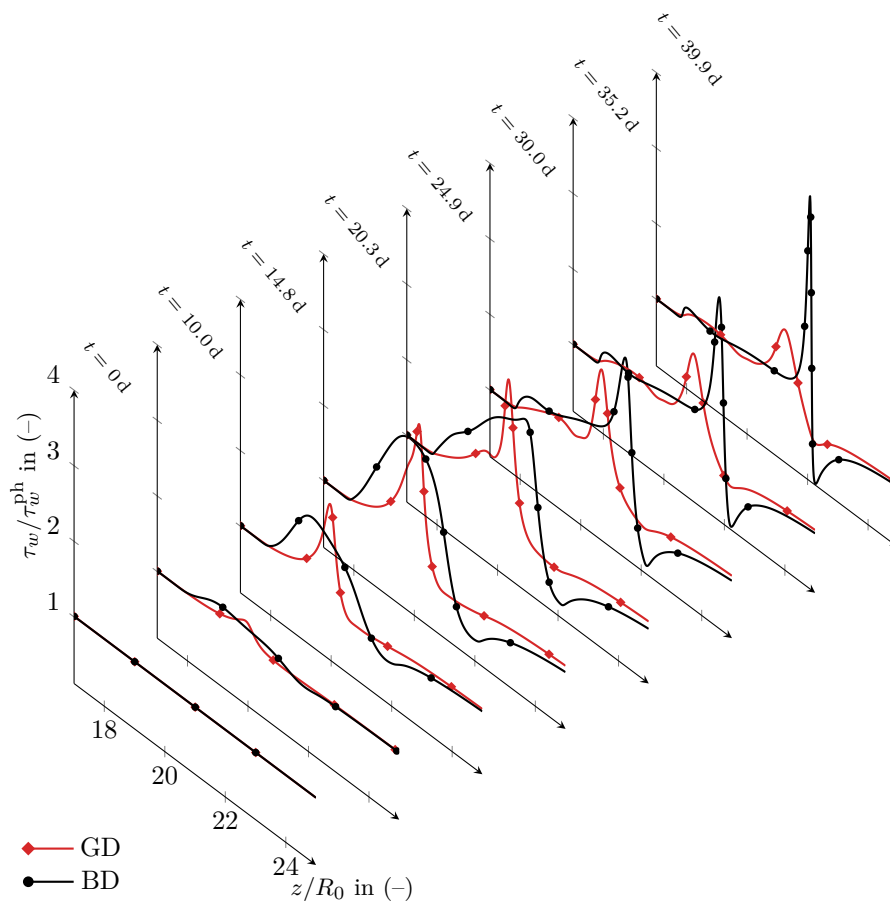


Fig. 8: Spatial variations of the normalized magnitude of the wall shear stress $\tau_w/\tau_w^{\text{ph}}$ for several arterial generations for gaussian (diamond symbols) and bump damage (circle symbols).

appears downstream of the maximums. The form of the initial damage over time determines the forms taken by the lesion during its development and the resulting WSS shapes. In the GD model, the lesion forms a rather intense peak up to $t = 20$ days (see Figure 5) and we find this form in the spatial variation of the WSS for $t = 10, 14.8, 20$ days with a lower wall shear stress zone downstream.

On the other hand, after 20 days, the locations of the lowest WSS exerted downstream of the initial damage are correlated, with a delay effect, with the zones of tissue growth responsible for the macroscopic lesion displacement (see Figure 5). After 20 days, the longitudinal distribution of WSS drives the lesion dynamics according to Figure 5 and 8. The other important result to be drawn from Figure 8 is that the displacement of the maximum of WSS, as well as its value, is exacerbated in the BD model compared to the GD model. This remark also applies to the minima of WSS which are lower in bump damage.

In order to quantify the displacement and the values of the extremum of WSS during the two models of damage, we follow respectively the trajectories of the maximum and the minimum of WSS at each arterial generation in the gaussian and bump damages, noted $\tau_w^{\text{max}}(t, z), \tau_w^{\text{min}}(t, z)$, in Figures 9 (a) and (b). In BD, the maximum of $\tau_w^{\text{max}}(t, z)$ appears during the phase of downstream displacement of the lesion (at $t = 47$ days at $z/R_0 \sim 22.3$), while it is observed at $t = 23$ days at $z/R_0 \sim 20.3$ in GD model. The minimum of $\tau_w^{\text{min}}(t, z)$ occurs in time and space in BD and GD respectively at $t \sim 39$ days and at $z/R_0 = 22.2$ and at $t = 52.7$ days and at $z/R_0 = 22.5$. The bump damage induce smaller WSS values, *e.g.* $\tau_w^{\text{min}}/\tau_w^{\text{ph}} < 0.2$, than the gaussian damage model. Moreover, according to this figure, no recirculation zone, detectable when $\tau_w^{\text{min}} = 0$, is generated during the development of the lesion in both models of damage. To quantify the delay between low levels of WSS and promotion of tissue growth predicted by our model, we compare the instant and location of the smallest WSS value in BD ($t \sim 39$

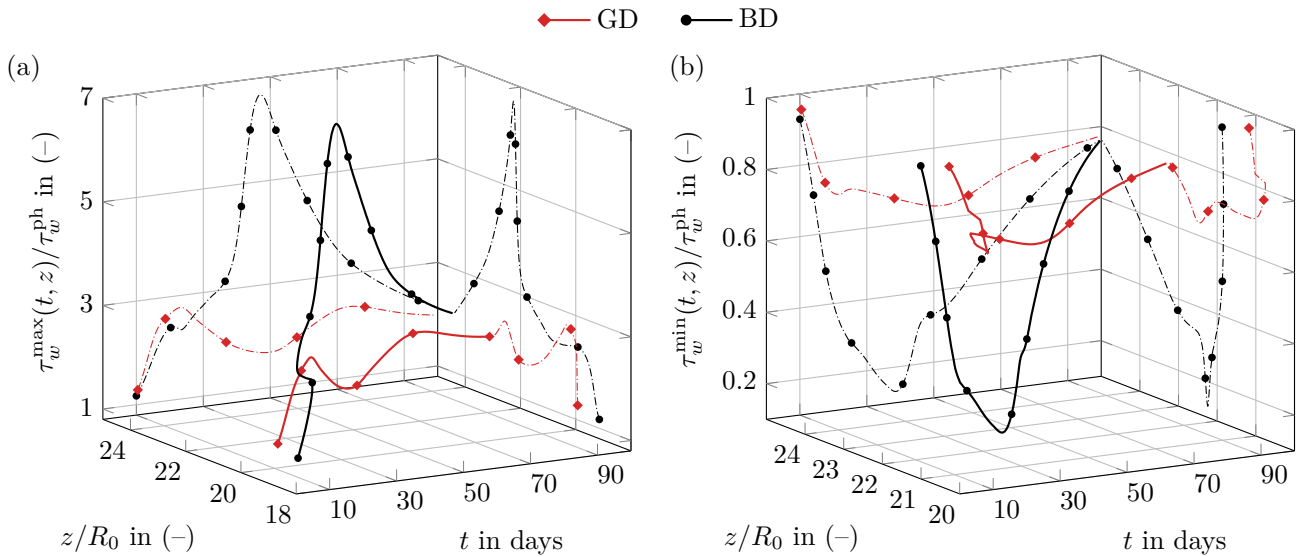


Fig. 9: Trajectories (solid lines) of the maximum (a) and minimum (b) normalized wall shear stress $\tau_w/\tau_w^{\text{ph}}$ during lesion development in the gaussian (diamond symbols) and the bump damage (circle symbols). For a clear visualization of these three-dimensional trajectories, projections are proposed on the planes $(z/R_0, \tau_w/\tau_w^{\text{ph}})$ and $(t, \tau_w/\tau_w^{\text{ph}})$ in dotted lines.

days at $z/R_0 = 22.2$) with the instant and location of the strongest stenosis ($t = 54.1$ days at $z = 22.5R_0$). We notice a time lag of about 15 days between these two events while spatially these two extremes coincide.

3.2 Spatio-temporal dynamics of tissues growth

3.2.1 Endothelium regeneration

We present the ECs response to the two models of damage. Figures 10 (a) and (b) show the spatio-temporal evolution of the ECs population in term of $E^\dagger(t, z)$, the rescaled EC count by its maximal value at each compartment as $E^\dagger(t, z) = E(t, z)/E_{\text{max}}(z)$. ECs follow a logistic dynamics not coupled with other variables of the model, thus Figure 10 presents different logistic dynamics for each compartment which differ only from the initial condition applied. Figure 10 (c) shows the dynamics of ECs regeneration at four longitudinal positions respectively at $z/R_0 = 20, 21, 22, 24$. The main difference between GD and BD cases is about the length of the severely damaged zone ($E^\dagger(t_0, z) < 0.5$ or $d(t_0, z) > 0.5$ with $d = 1 - E^\dagger$), according to our initial damage conditions defined in section 2.4. Depending on the initial level of damage, full re-endothelization is achieved between few hours (where $d_0 < 0.1$) and 14 days (where $d_0 = 0.99$) as seen in Figure 10 (c). The ranges of timescale of restoration of the EC layer, according to the degree of injury, is consistent with val-

ues reported in [12]. Endothelial regeneration in zones where $d_0 > 0.5$ being longer because of the logistic dynamics, we observe in the BD that a large part of the initially injured zone is still significantly damaged ($E^\dagger(t = 6\text{d}) < 0.5$) at $t = 6$ days compared to the GD case, where a thin band centred on $z/R_0 = 20$ still remains significantly damaged (Figure 10 (a)).

We assess the consequences of these two models of damage on the dynamics of vascular species below.

3.2.2 Functional properties of vSMCs

We discuss here the spatio-temporal evolution of functional properties of vSMCs linked with bioavailability of GFs and WSS stimuli [12]. Figure 11 presents in each row the time evolution of functional properties for GD and BD cases. The first two columns of plots show their isocontours in (z, t) plane, with a dashed line where SFPs is zero in order to show on/off switch or change of property sign. The third column of plots shows curves in time of the SFPs at relevant longitudinal positions along the artery.

The first row of Figure 11 presents the intimal dedifferentiation $c_i(t, z)$ of cSMCs into sSMCs for GD (a) and BD (b). The spatio-temporal evolution of c_i is globally the same for both damages with a switch on at the centre of damaged zone from the beginning of the simulation and a switch off around days 22 in this same region. In regions downstream the initial damages, and to a lesser extent upstream, c_i continue to be expressed

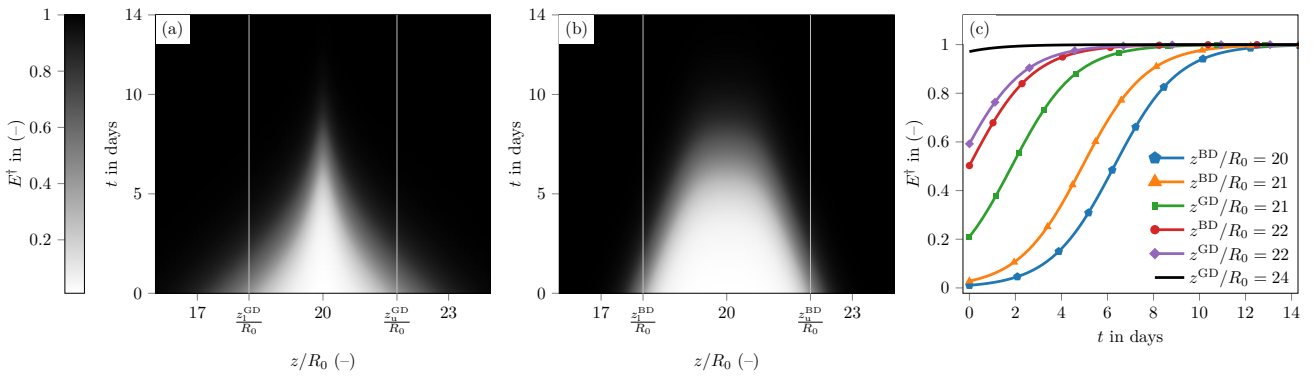


Fig. 10: Re-endothelization of the ECs in term of $E^\dagger(t, z) = E(t, z)/E_{\max}(z)$, the rescaled EC count by its maximal value at each compartment, in the first 14 days. For (a,b) plots, x -axis is the dimensionless longitudinal position z/R_0 and y -axis is time in days. (c) Time evolution of ECs at several longitudinal position.

(see contour of $c_i = 0$ in dashed line in Figure 11 (a) and (b)) with even an increase in its intensity. In the damaged zones, the time interval where c_i is switch on, by the use of MMFs, and the c_i intensity are the same for both models of damage and 1D case between 0 and 30 days (see Figure 11 (c)). The two differences between GD and BD can be seen in the length of the artery subject to pro-growth functional properties (greater in the BD case because of a strong damage more spread out) and in the dedifferentiation intensity downstream the damaged zones. The increase in dedifferentiation is stronger in the BD case than in GD case as seen in Figure 11 (c).

The second row of Figure 11 presents for GD (a) and BD (b) the migration of vSMC within intima layer $m_i(t, z)$. Migration intensity and time interval are equivalent for both cases but the length of the artery subject to migration is greater in BD, due to the nature of the BD denudation (see Figure 10). Note that unlike c_i , in any case migration (which use MMFs) is not triggered outside of the injury areas, whether it be downstream or upstream (see Figure 11 (a) and (b)). The non-switch on outside damaged zones is mainly due to the choice of threshold migration value $t_m = 1.8$, higher than threshold dedifferentiation value $t_c = 1.2$ (see [12] for parameter values). Figure 11 (c) compares migration rates in 1D case, GD and BD at $z/R_0 = 20, 21$. At $z/R_0 = 20$, all cases are equivalent in intensity and duration of the expression of migration, starting in all cases on day 3.5. The only slight difference is the end time of migration, that occurs earlier in bidimensional simulations.

The final row of Figure 11 concerns the turnover rate of sSMCs, *i.e.* proliferation minus apoptosis as $r_i = p_i - a_i$, for GD (g), BD (h) and a comparison of 1D case, GD and BD at positions $z/R_0 = 20, 22$ (i). As for migration and dedifferentiation processes, the main dif-

ference between GD and BD is about the length of the artery prone to cellular hyperplasia where $r_i > 0$, highlighted with an isocontour of $r_i = 0$ in Figure 11 (g,h). The $r_i = 0$ contour highlights, from approximately 15 days, the zone prone to hyperplasia and its motion downstream of the initial damage. This displacement is stronger with a higher intensity in BD case with $r_i > 0.1$ after 25 days (see Figure 11 (h,i)). After 30 days, almost all the zone initially damaged ($z/R_0 \in [19, 21]$) expresses negative turnover rates of sSMCs. Only the downstream zones have positive turnover rates (see Figure 11 (g,h,i)).

As in the 1D case, during the first two weeks, the imbalance between cellular proliferation and apoptosis leads to onset of lesions (seen Figure 5). At $z/R_0 = 20$, the instants when we switch from cellular growth into cellular loss are in the GD case at $t = 16$ days and in the BD case at $t = 18$ days. Both instants appear before that of 1D case at $t = 21$ days. In Figure 11 (i), we present the evolution of r_i in one downstream region of the initial damage at $z/R_0 = 22$. This region is slightly injured initially, *i.e.* $d_0 \leq 0.5$ (Figure 10), yet we observe an increase of the functional property in both GD and BD cases, with a greater one for BD case. This increase in the turnover rate of sSMCs is at the origin of the lesion development observed downstream of the initially damaged zone, visible in Figure 5, and it is due to the low WSS exerted in this zone over this time interval (see Figures 8 and 9 for $t \in [10, 30]$ days).

3.2.3 Dynamics of sSMCs

We show in Figure 12 the predicted sSMCs dynamics within intima and media layers between 0 and 100 days for the two considered cases. These dynamics presented in this section results directly from the spatio-

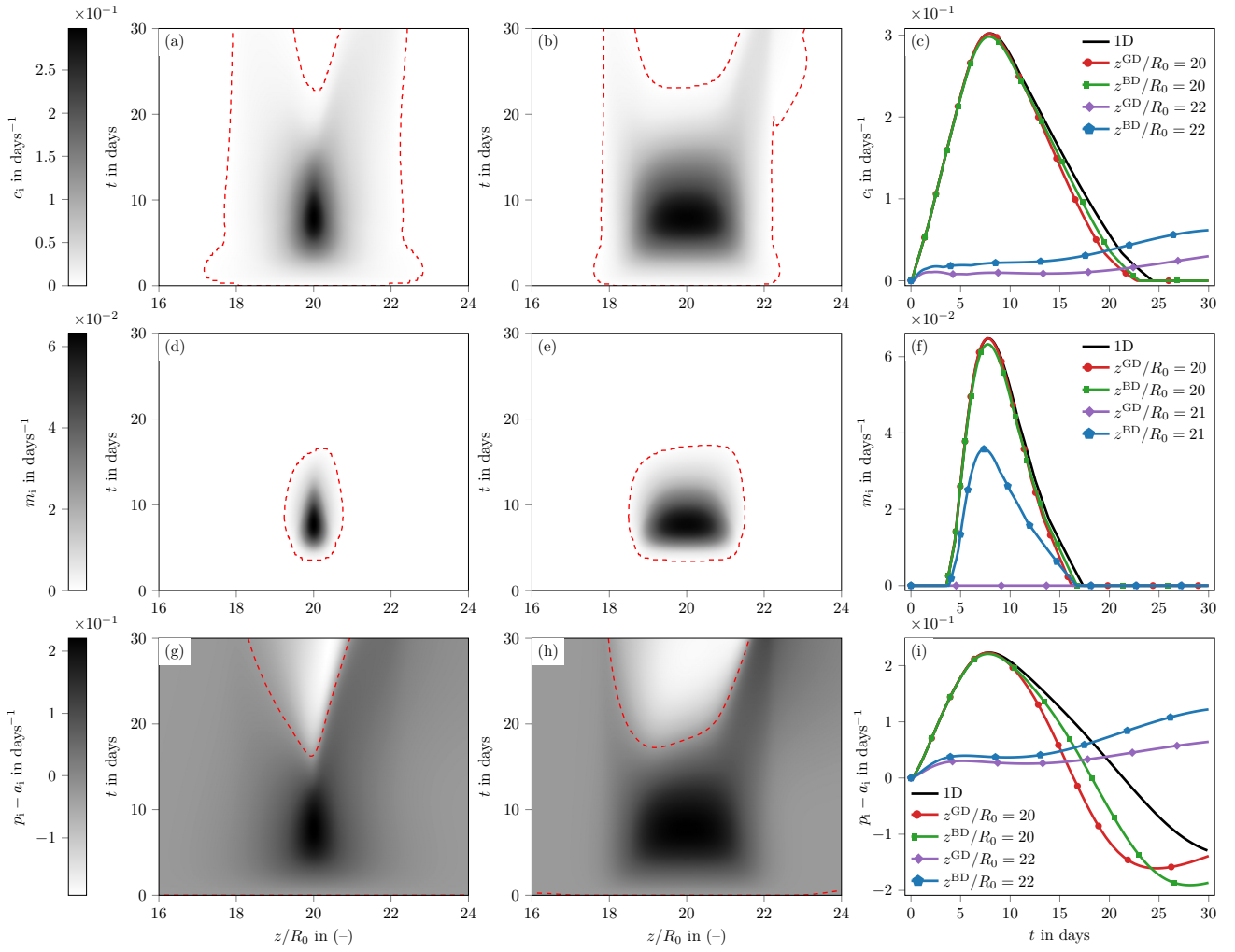


Fig. 11: Evolutions of the FPs of vSMCs in gaussian, bump and 1D case between 0 and 30 days. For (a,b,d,e,g,h) plots, x -axis is the dimensionless longitudinal position z/R_0 and y -axis is time in days. (c,f,i) Time evolution of FPs at several longitudinal position. Intimal dedifferentiation rate of vSMCs $c_i(t, z)$ in GD (a) and BD (b). Time evolution of c_i in 1D, GD and BD cases (c). Intimal migration rates of vSMCs $m_i(t, z)$ in GD (d) and BD (e). Time evolution of m_i in 1D, GD and BD cases (f). Intimal turnover of sSMCs $r_i(t, z)$ in GD (g) and BD (h). Time evolution of r_i in 1D, GD and BD cases (i).

temporal evolutions of their functional properties described above.

The first row of Figure 12 shows the intimal sSMCs dynamics through $S_i^\dagger(t, z)$, the counts of SMCs $S_i(t, z)$ divided by its initial-physiological compartmental count $S_i^{\text{ph}}(z)$. The two initial damages triggered a hyperplasia in the centre of the damaged zones at short timescale within $t < 20$ days. Rapidly, the lesions resorbed in the central region as seen in Figure 12 (c). These two phases of narrowing and enlargement, seen in the 1D case, are driven by SFPs dynamics which itself is driven by GFs dynamics and WSS stimuli. Important intimal hyperplasia in the regions downstream of the initial damages ($z/R_0 > 22$) is not seen in either GD or BD cases

whereas SFPs prone to tissue growth are expressed, *e.g.* the turnover rates $r_i^{\text{GD, BD}} > 0$ and dedifferentiation rates $c_i^{\text{GD, BD}} > 0$, which contribute to the definition of pathology-promoting zones. This lack of significant IH in these regions is due to the non-migration of cells from the media to the intima seen in Figures 11 (d,e,f). A further consequence of the non-expression of cell migration is the prediction of medial hyperplasia in the downstream areas which we are now discussing.

The second row of Figure 12 shows the normalized media count of sSMCs $S_m^\dagger(t, z)$. In both damages, we observe a spatio-temporal dynamics of a hyperplasia developing in the damaged zones at short timescale

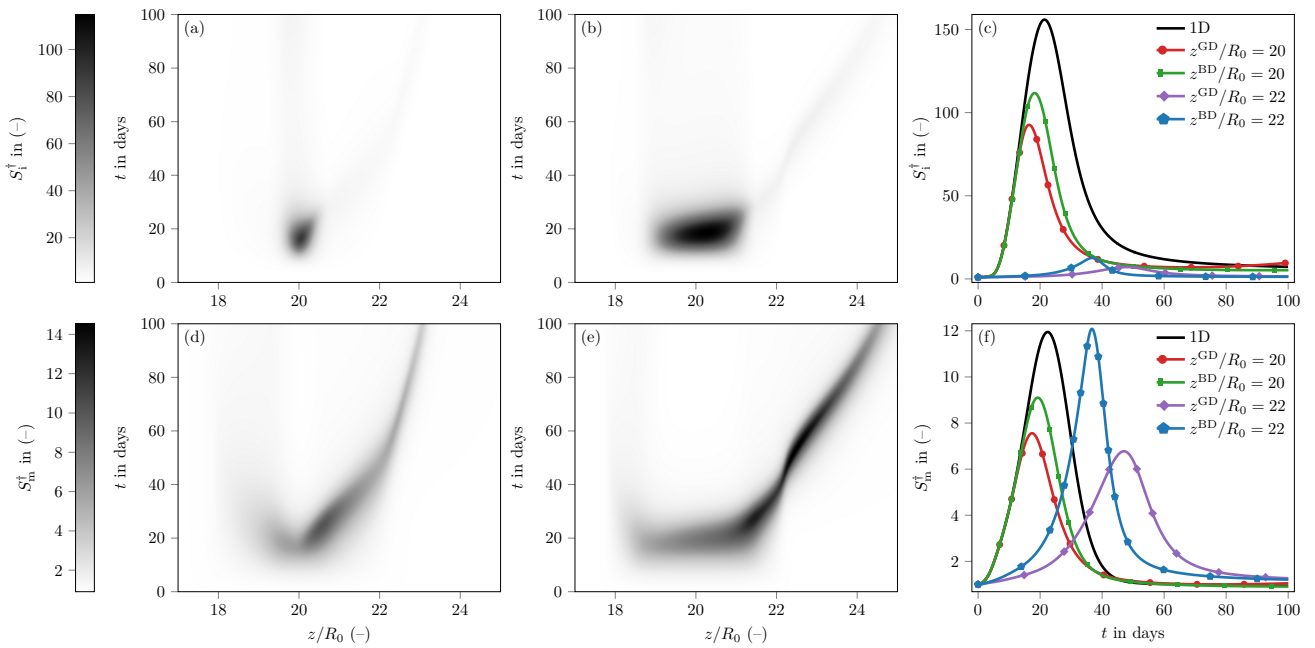


Fig. 12: Evolutions of intimal and medial rescaled sSMCs population, $S_{i,m}^{\dagger}$, in GD, BD and 1D case between 0 and 100 days. For (a,b,d,e) plots, x -axis is the dimensionless longitudinal position z/R_0 and y -axis is time in days. (c,f) Time evolution of $S_{i,m}^{\dagger}$ at several longitudinal positions. $S_{i,m}^{\dagger}$ in GD (a) and BD (b). Time evolution of $S_{i,m}^{\dagger}$ in 1D, GD and BD cases (c). S_m^{\dagger} in GD (d) and BD (e). Time evolution of S_m^{\dagger} in 1D, GD and BD cases (f).

(within $t < 20$ days) and then mainly moving downstream the initial damaged zones.

As described in [12], at short timescale, the formation of the lesion is due to the denudation of the endothelium which activates the functional properties pro-growth of vSMCs. The predicted intimal and medial hyperplasia phases in damaged zones are shorter and weaker than the one of 1D case (Figures 12 (c) and (f) at $z/R_0 = 20$). As seen in Figure 11 (i) for the intimal turnover, this is provoked by a shorter interval prone to cellular proliferation with $r_{i,m} > 0$. Note that the intensity of medial hyperplasia is maximal in downstream regions where initial endothelial damage was slight, *i.e.* $d_0 \leq 0.5$ (see Figure 10). The maxima of medial sSMCs are for GD $S_m^{\dagger,\max}(t = 24.57\text{d}, z/R_0 = 20.59) = 10.89$ and for BD $S_m^{\dagger,\max}(t = 52.28\text{d}, z/R_0 = 22.46) = 14.54$.

The narrowing phases downstream the initial damage — discussed in section 3.1.1, for BD in $z^{\text{BD}}/R_0 \in [22, 22.6]$ and for GD in $z^{\text{BD}}/R_0 \in [22.2, 22.4]$ (see in Figure 4) — are the consequence of the spatio-temporal evolutions of sSMCs presented in this section. In both models of damage, the increase of r_i and switch on of c_i in the downstream region of the initial damage promote tissue growth and are due to the WSS distribution which have, because of the lesion development, values lower than the physiological one ($\tau_w/\tau_w^{\text{ph}} < 1$) (see Fig-

ure 8 and 9). In that type of flow regions, it is known that production of GFs by ECs and permeability to plasma molecules are disturbed, which is called “*endothelial dysfunctions*” [16]. Our model succeeded in reproducing the characteristics of a pathology-promoting zone, with $r_i > 0$ and $c_i > 0$, in both intima (see Figure 11) and media (data not shown), thanks to the multiple assumptions made at various spatial and temporal scales [12]. The only functional property not expressed in downstream regions is the migration. We have chosen a threshold value for migration of $t_m = 1.8$ to fit experimental finding about cellular migration starting around $t \in [2, 4]$ days [12]. Regarding the absence of intimal hyperplasia in downstream developing lesions, a inferior value will permit to express this cellular functional property, *e.g.* the value of $t_m = 1.2$ has been tested and has permitted to predict a intimal hyperplasia in downstream regions in both type of damages [11].

By comparing the predictions of the IH model according to the two types of damage, we observe a tissue growth strongly modulated by the morphology of the stenosis. Indeed, we note that in the presence of a stenosis having a smooth and diffuse morphology, like that induced by GD at $t = 20$ days (see Figure 5 (c)), the hyperplastic response of the model downstream of this stenosis is less than that produced by the initial disendothelization. On the contrary, for a stenosis having

a stiff and focal morphology, such as that induced by the BD at $t = 20$ days (see Figure 5 (d)), the hyperplastic response downstream of this stenosis is of a similar intensity to that induced by disendothelization.

3.2.4 Composition of lesions

Figure 13 shows the spatio-temporal evolution of the intimal layer composition in terms of the volume fraction $\varphi_i(t, z)$ of vSMCs and ECM (collagen in our model) for the two models of damage. From initial time until 12 months post-damage, we present the overall evolution as well as temporal evolutions at several characteristic longitudinal positions in Figures 13 (e,f) compared to 1D test-case results.

For each initial disendothelization, respectively in Figures 13 (a,c) for GD and in Figures 13 (b,d) for BD, we follow the maturation process of the lesion along the artery. As in our monodimensional test-case, during the lesion formation, we observe an intima layer that is more cellular than fibrous. Over time and especially in the centre of the initially damaged zone ($19 < z/R_0 < 21$), the intima becomes more fibrous and less cellular.

In both damages at the centre of the damaged zone ($z/R_0 = 20$), during the first 20 days, the dynamics of volume fraction obtained in axisymmetric configuration is identical to that of 1D case (see Figures 13 (e,f)). However, between 1 and 12 months, the maturation process of the lesion is different between 1D and axisymmetric configuration in both damages. Despite these different behaviours, after one year in the GD and BD cases, the lesion in the centre of the injury has an equivalent composition to that of the 1D test-case and the experiments from the literature, *i.e.* 80% of ECM and 20 % of vSMCs [12].

Figure 13 informs also about the continuous downstream displacement of the lesion which is indicated by arrows in Figures 13 (a,b,c,d). At 12 months, the developing intimal hyperplasia in GD and BD cases are respectively at $z/R_0 \sim 24.8$ and $z/R_0 \sim 28$ (see Figures 13 (a,b)). Over the same duration of 12 months, BD case presents a higher continuous downstream displacement of the incipient lesion than the GD case. Thus, the displacement velocity is greater in the BD case compared to the GD case. During the first year post-damage, in both disendothelization models, the lesion displacement velocity decreases among time, *e.g.* during the first 100 days (~ 3.3 months), the maximum volume fraction of vSMCs moves in GD and BD cases respectively by $3R_0$ and $4.5R_0$, while during the last 265 days (~ 8.8 months), the maximum moves in GD and BD cases respectively by $1.83R_0$ and $3.5R_0$ (see Figures 13 (a,b)).

Downstream of the initial zone of damage, we find for the volume fraction of vSMCs an increase leading to a maximum then a decrease until the stabilization of φ_i^{vSMC} . The inverse dynamics is visible for φ_i^{ECM} . It is interesting to underline that downstream of the initial damage, and contrary to what occurs at the centre, the lesions in both types of injury are all, after one year, more composed of vSMCs than of ECM, *i.e.* $\varphi_i^{\text{vSMC}}(t, z/R_0 \geq 22) > \varphi_i^{\text{ECM}}(t, z/R_0 \geq 22)$. This characteristic composition arises from an absence of strong intimal hyperplasia at short timescale. Indeed, in order to obtain a lesion mainly composed of collagen at long timescale, it is essential that a strong proliferation of vSMCs be expressed. We notice that each peak of φ^{vSMC} precedes a strong increase in the volume fraction of collagen φ^{ECM} . This is particularly clearly visible in axisymmetric configuration for both damages in Figures 13 (e,f) at $z/R_0 = 20$.

4 Conclusion and perspectives

In the present work, we apply our multiscale model of intimal hyperplasia to an axisymmetric artery in which a steady hemodynamics is considered. The spatio-temporal evolution of two types of lesion has been simulated considering two models of disendothelization.

By considering two models of damage, we assess the influence of this initial condition on the spatio-temporal evolution of the lesion. The two damages, focal for the bump damage (BD), and diffuse for the gaussian damage (GD), induce, in the disendothelized zone, similar lesions in terms of morphology and composition. In these central zones, focal- or diffuse-type hyperplastic lesions develop over a period of 20 days post-damage. Then, these hyperplasia vanish and the lesions become more and more fibrous.

According to all our comparisons of the 1D and axisymmetric cases, the main results validating the model in 1D test-case are observed in an axisymmetric artery at the centre of the damaged zone. By this comparison, we ensure the non-regression of the axisymmetric prediction compared to the validated results in 1D [12]. These main results found in the central damaged zone of our axisymmetric artery ($z/R_0 = 20$) are: a short-lived intimal hyperplasia causing a predominantly cellular lesion; long-term maturation inducing a predominantly fibrous lesion with 80% of ECM and 20 % of vSMCs. However, due to a more realistic geometrical configuration, the dynamics predicted by the axisymmetric artery at $z/R_0 = 20$ is slightly different from that of the 1D case.

After the 20th day, while the stenosis is maximal in the injured zones, our IH model predicts a new hyper-

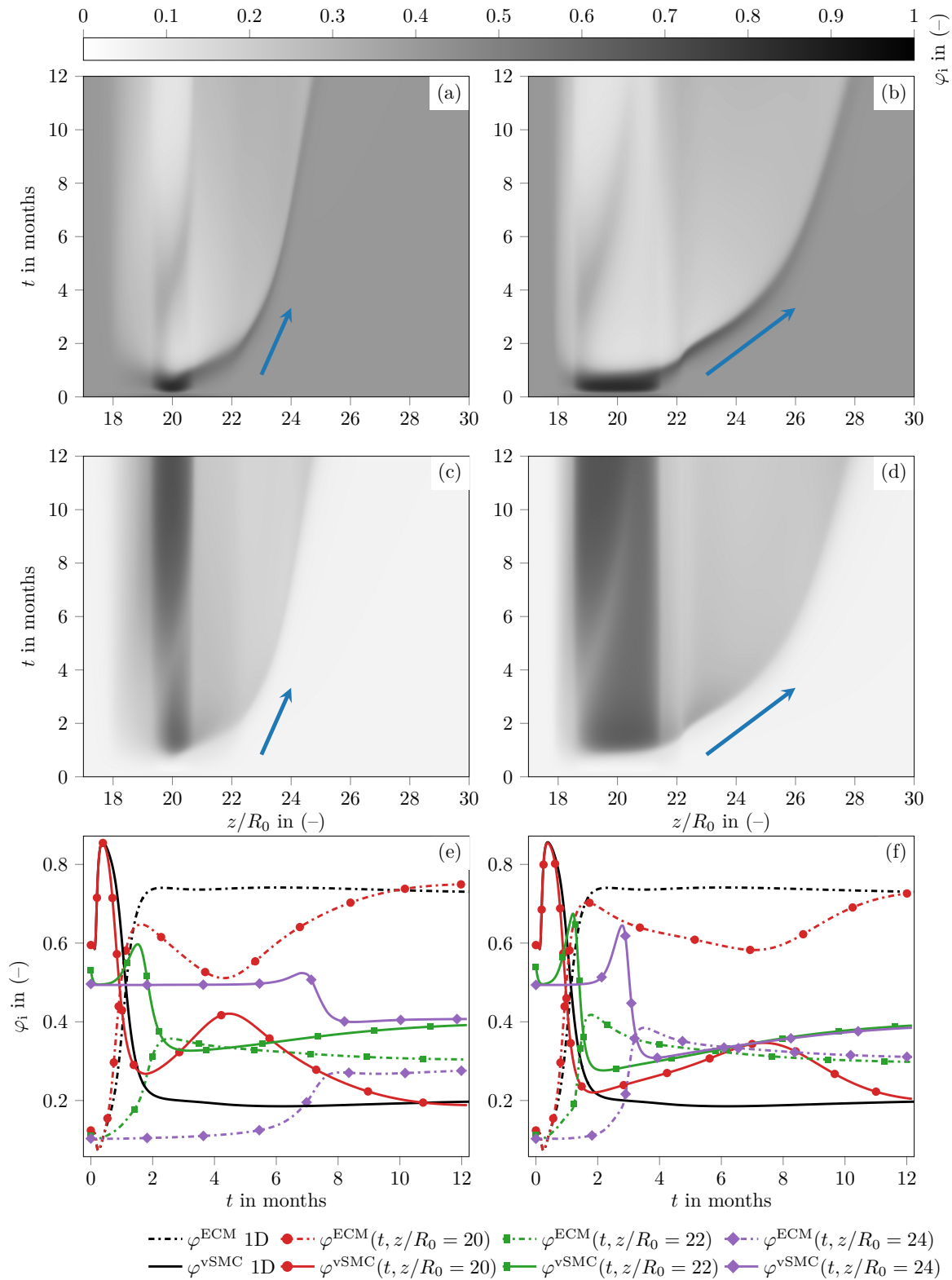


Fig. 13: Evolutions of intimal volume fractions $\varphi_i(t, z)$ of vSMCs and ECM between 0 and 12 months. For (a,b,c,d) plots, x -axis is the dimensionless longitudinal position z/R_0 and y -axis is time in months. (e,f) Time evolution of $\varphi_i(t, z)$ at several longitudinal positions. $\varphi_i^{\text{vSMC}}(t, z)$ in GD (a) and BD (b). $\varphi_i^{\text{ECM}}(t, z)$ in GD (c) and BD (d). Time evolution of φ_i between 1D/GD cases (e) and between 1D/BD cases (f).

plastic development downstream of the stenosis in BD and GD. This downstream tissue growth is induced by zones of low WSS downstream of the stenosis caused by initial disendothelization. Our two simulations succeed to capture accurately the downstream development of lesion thanks to the automatic remodelling criteria which permit to overcome constant remodelling intervals by considering remodeling frequencies dependent on lesion dynamics. Macroscopically, the sensitivity of the model to pathology-promoting and pathology-protective zones is qualitatively consistent with experimental results [20, 15]. This consistency only results from the modelling of biological and biochemical hypotheses made at the cellular scale [12].

As seen in our two simulations, the maturation process of IH lesions is well captured by our modelling because it is a direct consequence of concurrency of three modeled mechanisms of promotion/inhibition of IH [15], production of collagen fiber by sSMCs and arterial remodeling. At short timescale, the model predicts an incipient stenosis mainly cellular. Thus, because of the growing stenosis and narrowing remodeling events in the injured zone, the WSS increases which inhibit cellular growth over time. At the same time, downstream the damaged zone, the WSS decrease below physiological value which promote cellular growth. As we consider a loose coupling between hemodynamics and arterial remodeling, in both cell decrease or growth phases, remodeling events of the arterial lumen permit to modulate biochemical, cellular and fibrotic dynamics.

Nevertheless, we could not quantitatively validate the predictions of our model in terms of downstream lesion displacement resulting from the consistency of areas of high and low levels of WSS. Indeed, to our knowledge, there are no experimental data on the spatio-temporal evolution of intimal hyperplasia lesion that we could transpose to the *in silico* experiences of idealized arteries undergoing disendothelizations proposed in this work.

Lesion displacement is predicted in both damages following the appearance of lesions in the initially disendothelized zones. The lesion moves continuously downstream with a speed of movement influenced mainly by the morphology of the stenosis. This displacement is self-sustained over time by both the high WSS levels in the zone of maximum stenosis promoting tissue decrease on the one hand, and on the other hand, downstream of the stenosis by the low WSS promoting tissue growth.

According to the simulations presented in this article, the initial damage plays a central role in the genesis of intimal hyperplasia, while the local WSS controls the spatio-temporal evolution of the lesion after its onset.

Thus, we found that the morphology of the stenosis strongly influences the spatial variation of WSS, which in turn affects the dynamics of the tissue growth: a smooth and diffuse stenosis morphology, as seen during GD lesion development, results in less hyperplastic response than stiff and focal stenosis morphology, induced during the BD lesion development.

Our study opens the following perspectives by suggesting possible improvements of the model.

Firstly, given the importance of endothelial damage and regeneration on lesion development, the model could be enriched by taking into account hemodynamical influence of WSS on the dynamics of endothelial cells as reviewed in [14, 3]. This improvement is totally feasible in our modelling by considering a WSS-dependent proliferation rate in our equation for ECs dynamics which may slow or accelerate proliferation depending on flow conditions. As the process of regeneration of ECs drives the genesis of IH, we assume that this improvement of the model could be of great interest.

Given the good agreement of (a) our axisymmetric results in the central damage zone compared to our 1D case validated, and (b) the prediction of the model regarding the concept of pathology promotion and protection zones, new *in silico* experiments are called for to provide insights of IH development all along the arterial tree. These experiments will have to consider different flow regimes, geometrical configurations and initial structures of the arterial wall regarding the type of artery. The latter point will be challenging as geometrical and cellular properties along the arterial tree are scarce in literature.

5 Acknowledgments

Numerical simulations were carried out using the facilities of the PMCS2I of École Centrale de Lyon. We gratefully thank the entire staff of PMCS2I for the technical support, and especially Laurent Pouilloux for his infallible help.

A Reproducibility data, computational costs and sensitivity analysis

For the sake of further studies, we present in this section the reproducibility data in Tables 2 and 3 and the computational costs of our two disendothelization models simulations.

Numerical simulations were carried out in parallel on twelve processors of the PMCS2I of École Centrale de Lyon. The simulations lasted 1.17 days and 3.96 days respectively for the bump damage (BD) and the gaussian damage (GD). The axisymmetric artery geometry is more CPU time consuming than the one in monodimensional artery. For information, the computational cost of 1D test-case in [12] is about 0.2 minutes.

Because of the prohibitive computational cost of the axisymmetric cases compared to the 1D test-case, we perform a sensitivity study of the parameters of our model only in the 1D configuration. In [11, section 6.2], we propose a qualitative and quantitative exploration of the parameter space of our model using a methodology that nests two Global Sensitivity Analysis (GSA) methods. The realization of such sensitivity analysis methods in axisymmetric geometry could not have been achieved because of its computational cost.

B Mesh convergence study

In this section, we present the convergence studies used to set relevant mesh parameters for the presented simulations. These parameters define the meshes of the luminal domain linked to CFD and of the parietal domain linked to the model of intimal hyperplasia. An illustration of the mesh parameters of domains is proposed in Figure 14 (d). The convergence studies were carried out on the gaussian damage (GD). The fixed and variable parameters of each study are presented in Table 4.

A first study, shown in Figure 14 (a), impose conformed meshes between luminal and parietal meshes to choose the relevant discretization in the damaged zone of parietal mesh. This figure shows, as a function of the number of parietal mesh points in the central zone of the GD case, N_{TG}^M (see Figure 14 (d)), the relative error of luminal radius at $t = 60$ days, *i.e.* $R_1(z, t = 60d)$, based on a finer mesh which has $N_{TG}^M = 1301$. From this study, we choose $N_{TG}^M = 1001$.

As the whole coupling between hemodynamics and tissue growth is based on the WSS distribution, and regarding the strong influence of WSS on vascular species dynamics (see Figure 12), the most limiting factor for an accurate simulation of a spatio-temporal lesion evolution is the WSS computation. The more the hemodynamics will be finely resolved in the near endothelium region, the more precise the WSS will be obtained, within the feasible simulation limit.

In order to evaluate the influence of the numerical resolution of hemodynamics in axisymmetric configuration, two parameters of the luminal mesh were tested: discretization in the radial direction and discretization in the longitudinal direction.

Table 1: **OpenFOAM** boundary conditions used at boundaries of the luminal axisymmetric domain Ω_1 shown in Figure 1. **parabolicInletVelocity** is custom boundary condition of a Poiseuille velocity profile from (2a).

	u	p
Inlet Γ_1^{in}	parabolicInletVelocity	zeroGradient
Outlet Γ_1^{out}	pressureInletOutletVelocity	fixedValue 0
Endothelium Γ_1^e	fixedValue (0 0 0)	zeroGradient
Wedges $\Gamma_1^{w,0,1}$	wedge	wedge

Table 2: Numerical schemes of **OpenFOAM** used for spatial and temporal discretisation of equations (1).

dDtSchemes	gradSchemes	divSchemes	laplacianSchemes	interpolationSchemes	snGradSchemes
steadyState	leastSquares	bounded Gauss linearUpwind grad(U)	Gauss linear corrected	linear	corrected

Table 3: Definitions, values and units of the parameters of the model in a axisymmetric artery configuration. The parameters are grouped in several topics sections. For other parameters not specified in this table, refer to Tables in [12]. All the parameter values displayed in this table have been chosen. For mesh parameters, an illustration of meshes is shown in Figure 14 (d).

Constant	Description	Value	Units
Geometry of the axisymmetric artery			
R_0	Initial luminal radius	4×10^{-3}	m
R_{ext}	External wall radius	4.5×10^{-3}	m
L_I	Arterial inlet zone length	$15 R_0$	m
L_M	Arterial central zone length	$15 R_0$	m
L_O	Arterial outlet zone length	$15 R_0$	m
Others parameters see [12, Table 1]			
Models of disendothelization			
z_G	Center of the damaged zone	8×10^{-2}	m
σ_G	Damage length control parameter	6×10^{-3}	m
z_1^{BD}	Lower limit of damage	7.2×10^{-2}	m
z_u^{BD}	Upper limit of damage	8.8×10^{-2}	m
δ_z	Transition length parameter	2×10^{-3}	m
Hemodynamics			
Re_0	Initial Reynolds number	3.0×10^2	–
Others parameters see [12, Table 1]			
Intimal hyperplasia model			
l_M	Half smoothing distance of the MMF	5×10^{-2}	–
Others parameters see [12, Table 1]			
Temporal integration			
t_0	Initial time	0	day
t_f	Final time	365	day
d_0	Maximum initial damage parameter	9.9×10^{-1}	–
\mathbf{y}_0	Initial conditions	†	
\mathbf{h}_0	History conditions	†	
Others parameters see [12, Table 1]			
Parietal mesh			
$N_{TG}^{I,O}$	Number of parietal point in inlet and outlet arterial zones of length $L_{I,O}$	2	–
N_{TG}^M	Number of parietal point in the central arterial zone of length L_M	1001	–
N_{TG}	Total number of parietal compartments	1002	–
Luminal mesh			
$N_z^{I,O}$	Number of luminal point in the longitudinal direction at inlet/outlet arterial zones of length $L_{I,O}$	401	–
N_z^M	Number of luminal point in the longitudinal direction at the central arterial zone of length L_M	7000	–
N_y	Number of luminal point in the radial direction.	51	–
Δ_y	Thickness of the near endothelium cell	2×10^{-5}	m
N^{cell}	Total number of cells in the luminal mesh	389950	–
CFD boundary condition			
u_{max}	Maximal velocity at inlet	2.45×10^{-1}	$m s^{-1}$
$R_{i,in}$	Inlet radius	4×10^{-3}	m
p_{out}	Outlet pressure	0	Pa
CFD resolution parameters			
N_{nnO}	Number of SIMPLE explicit non-orthogonal correction	4	–
p^r	Pressure residual tolerance	1×10^{-6}	–
\mathbf{u}^r	Velocity residual tolerance	1×10^{-6}	–
N_{max}	Maximal number of SIMPLE iterations	1000	–
α_u^e	Velocity equation relaxation factor	0.7	–
α_p^e	Pressure equation relaxation factor	0.7	–
α_u^f	Velocity field relaxation factor	1	–
α_p^f	Pressure field relaxation factor	0.3	–

† Calculated from volume fractions of [12, Table 4]. Initial conditions and histories are functions of the volumes of compartments.

Table 4: Summary of the parameters of the luminal and parietal meshes in the three convergence studies proposed in Figure 14. For an illustration of the construction of luminal and parietal meshes from these parameters, see Figure 14 (d).

Fixed parameters	Variable parameters
Conform meshes case (see Figure 14 (a))	
$N_y = 31, \Delta_y = 2 \times 10^{-5} \text{ m}, N_z^{I,O} = 401, N_{TG}^{I,O} = 2,$	$N_{TG}^M \in [201, 1301]$ and $N_z^M = N_{TG}^M$
Variation in the radial direction for luminal mesh (see Figure 14 (b))	
$N_z^M = 1000, N_z^{I,O} = 201, \Delta_y = 1 \times 10^{-5} \text{ m}, N_{TG}^{I,O} = 2, N_{TG}^M = 1000$	$N_y \in [11, 51]$
Variation in the longitudinal direction for luminal mesh (see Figure 14 (c))	
$N_z^{I,O} = 201, N_y = 32, \Delta_y = 1 \times 10^{-5} \text{ m}, N_{TG}^{I,O} = 2, N_{TG}^M = 1000$	$N_z \in [1000, 7000]$

Imposing a constant radial compression of the luminal mesh with a thickness of the near endothelium cell of $\Delta_y = 1 \times 10^{-5}$ m, we study the influence of the number of points N_y and N_z^M respectively in Figure 14 (b) and (c). In Figure 14 (b), we observe a strong dependence of the number of points of mesh in the radial direction, with constant radial compression. From this study, we choose $N_y = 51$. Fixing $N_{TG}^M = 1000$, the Figure 14 (c) shows the influence of the increase in the longitudinal discretization of the luminal mesh on the relative errors of the luminal radius at $t = 60$ days, based on the finer luminal mesh with $N_z^M/N_{TG}^M = 8$. From this study, we impose the ratio $N_z^M/N_{TG}^M = 7$.

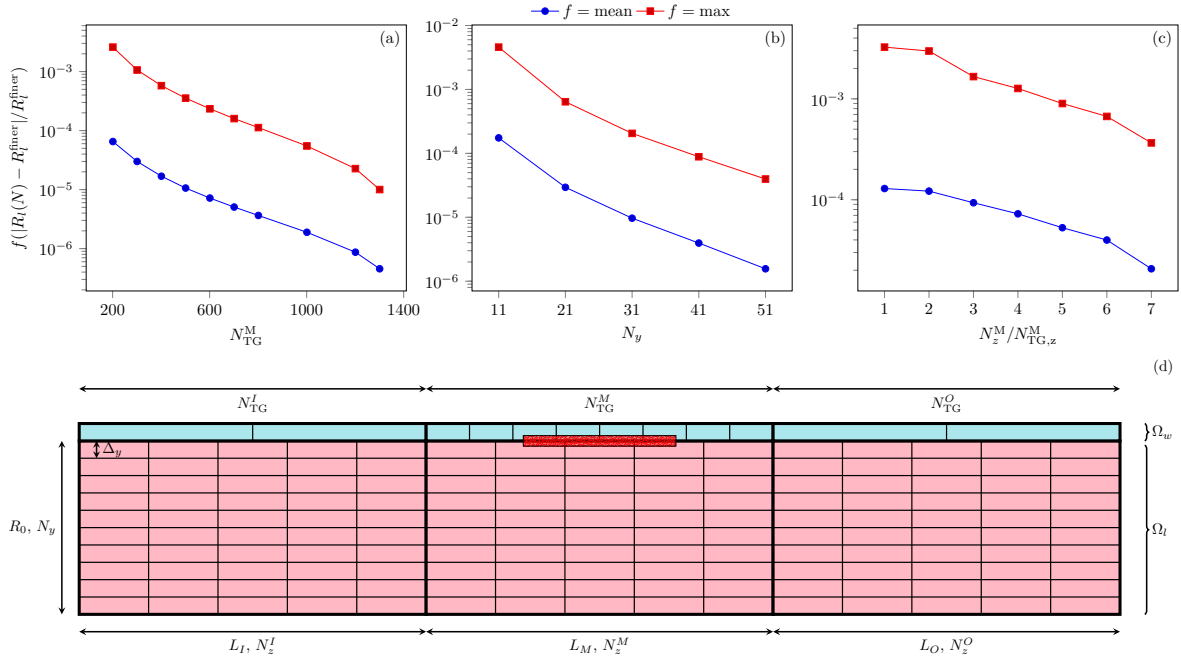


Fig. 14: Means and maximums of the relative error based on luminal radius at $t = 60$ days with respect to the finer mesh in the gaussian damage. The fixed and variable parameters of each study are shown in Table 4. (a) Relative errors as a function of the number of points in the longitudinal direction in the central zone N_z^M . The finer mesh has $N_z^M = 1301$ points. This study impose conform meshes between luminal and parietal domains. (b) Relative errors as a function of the number of points in the radial direction on the luminal mesh N_y . The finer mesh has $N_y = 51$ points. This study impose constant radial compression of the luminal mesh. (c) Relative errors as a function of the ratio between the number of longitudinal points of luminal and parietal meshes for $N_{TG}^M = 1000$. (d) Illustration in the plane of symmetry of the artery of the meshes in the luminal and parietal domains with the various mesh parameters considered. A hatched rectangle with red lines shows the initially damaged zone limited.

References

1. V. Calvez, J.G. Houot, N. Meunier, A. Raoult, and G. Rusnakova. Mathematical and numerical modeling of early atherosclerotic lesions. *ESAIM: Proc.*, 30:1–14, 2010. doi: 10.1051/proc/2010002.
2. A. Carrel and C.C. Guthrie. Results of the biterminal transplantation of veins. *The American Journal of the Medical Sciences*, 132:415–422, 1906.
3. D.A. Chistiakov, A.N. Orekhov, and Y.V. Bobryshev. Effects of shear stress on endothelial cells: go with the flow. *Acta Physiologica*, 219(2):382–408, 2016. doi: 10.1111/apha.12725.
4. M. Cilla, E. Peña, and M.A. Martínez. Mathematical modelling of atheroma plaque formation and development in coronary arteries. *Journal of the Royal Society, Interface*, 11 90:20130866, 2014.
5. A. Corti, C. Chiastra, M. Colombo, M. Garbey, F. Migliavacca, and S. Casarin. A fully coupled computational fluid dynamics — agent-based model of atherosclerotic plaque development: Multiscale modeling framework and parameter sensitivity analysis. *Computers in Biology and Medicine*, 118:103623, 2020. doi: 10.1016/j.compbiomed.2020.103623.
6. F. Donadoni, C. Pichardo-Almarza, M. Bartlett, A. Dardik, S. Homer-Vanniasinkam, and V. Díaz-Zuccarini. Patient-specific, multi-scale modeling of neointimal hyperplasia in vein grafts. *Frontiers in Physiology*, 8:226, 2017. doi: 10.3389/fphys.2017.00226.
7. J. Escuer, M.A. Martínez, S. McGinty, and E. Peña. Mathematical modelling of the restenosis process after stent implantation. *Journal of The Royal Society Interface*, 16(157): 20190313, 2019. doi: 10.1098/rsif.2019.0313.
8. M.H. Friedman, G.M. Hutchins, C. Brent Barger, O.J. Deters, and F.F. Mark. Correlation between intimal thickness and fluid shear in human arteries. *Atherosclerosis*, 39 (3):425–436, 1981. doi: 10.1016/0021-9150(81)90027-7.
9. C. Geuzaine and J.F. Remacle. Gmsh: A 3-D finite element mesh generator with built-in pre- and post-processing facilities. *International Journal for Numerical Methods in Engineering*, 79(11):1309–1331, 2009. doi: 10.1002/nme.2579.
10. M.E. Goodman, X.Y. Luo, and N.A. Hill. Mathematical model on the feedback between wall shear stress and intimal hyperplasia. *International Journal of Applied Mechanics*, 8(7), 2016.
11. J. Jansen. *Modélisation et simulation de l'écoulement hémodynamique couplé à la croissance tissulaire de l'endofibrose artérielle dans l'artère iliaque*. PhD thesis, Université de Lyon, 2021.
12. J. Jansen, X. Escrive, F.S. Godeferd, and P. Feugier. Multiscale bio-chemo-mechanical model of intimal hyperplasia. *Biomechanics and Modeling in Mechanobiology*, 21: 709–734, 2022. doi: 10.1007/s10237-022-01558-5.
13. R. Khosravi, A.B. Ramachandra, J.M. Szafron, D.E. Schiavazzi, C.K. Breuer, and J.D. Humphrey. A computational bio-chemo-mechanical model of in vivo tissue-engineered vascular graft development. *Integrative Biology*, 12(3): 47–63, 2020. doi: 10.1093/intbio/zyaa004.
14. Y.S.J. Li, J.H. Haga, and S. Chien. Molecular basis of the effects of shear stress on vascular endothelial cells. *Journal of Biomechanics*, 38(10):1949–1971, 2005. doi: 10.1016/j.jbiomech.2004.09.030.
15. V. Peiffer, S.J. Sherwin, and P.D. Weinberg. Does low and oscillatory wall shear stress correlate spatially with early atherosclerosis? a systematic review. *Cardiovascular Research*, 99(2):242–250, 2013. doi: 10.1093/cvr/cvt044.
16. J. Qiu, Y. Zheng, J. Hu, D. Liao, H. Gregersen, X. Deng, Y. Fan, and G. Wang. Biomechanical regulation of vascular smooth muscle cell functions: from *in vitro* to *in vivo* understanding. *Journal of The Royal Society Interface*, 11 (90):20130852, 2014. doi: 10.1098/rsif.2013.0852.
17. L.F. Shampine and S. Thompson. *Numerical Solution of Delay Differential Equations*, pages 1–27. 2009. doi: 10.1007/978-0-387-85595-0_9.
18. V.M. Subbotin. Analysis of arterial intimal hyperplasia: review and hypothesis. *Theoretical Biology and Medical Modelling*, 4(1), 2007. doi: 10.1186/1742-4682-4-41.
19. The OpenFOAM Foundation. *OpenFOAM v5 User Guide*. OpenCFD Ltd., 5.0 edition, 2017.
20. J.J. Wentzel, F.J.H. Gijzen, N. Stergiopoulos, P.W. Serruys, C.J. Slager, and R. Krams. Shear stress, vascular remodeling and neointimal formation. *Journal of Biomechanics*, 36(5):681–688, 2003. doi: 10.1016/S0021-9290(02)00446-3.